Research Article

TiO$_2$/Cu$_2$O/CuO Multi-Nanolayers as Sensors for H$_2$ and Volatile Organic Compounds: An Experimental and Theoretical Investigation

Oleg Lupan,* David Santos-Carballal,* Nicolai Ababii, Nicolae Magariu, Sandra Hansen,* Alexander Vahl, Lukas Zimoch, Mathias Hoppe, Thierry Pauporté, Vardan Galstyan, Victor Sontea, Lee Chow, Franz Faupel,* Rainer Adelung,* Nora H de Leeuw, and Elisabetta Comini

Cite This: ACS Appl. Mater. Interfaces 2021, 13, 32363−32380

Read Online

ACCESS | Metrics & More | Article Recommendations | SI Supporting Information

ABSTRACT: TiO$_2$/Cu$_2$O/CuO multi-nanolayers highly sensitive toward volatile organic compounds (VOCs) and H$_2$ have been grown in various thicknesses by a cost-effective and reproducible combined spray−sputtering−annealing approach. The ultrathin TiO$_2$ films were deposited by spray pyrolysis on top of sputtered−annealed Cu$_2$O/CuO nanolayers to enhance their gas sensing performance and improve their protection against corrosion at high operating temperatures. The prepared heterostructures were investigated using scanning electron microscopy (SEM), X-ray diffraction (XRD), and ultraviolet visible (UV−vis) and micro-Raman spectroscopy. The gas sensing properties were measured at several operating temperatures, where the nanolayered sensors with oxide thicknesses between 20 and 30 nm (Cu$_2$O/CuO nanolayers) exhibited a high response and an excellent selectivity to ethanol vapor after thermal annealing the samples at 420 °C. The results obtained at an operating temperature of 350 °C demonstrate that the CuO/Cu$_2$O nanolayers

with thicknesses between 20 and 30 nm are sensitive mainly to ethanol vapor, with a response of ∼150. The response changes from ethanol vapors to hydrogen gas as the thickness of the CuO/Cu$_2$O nanolayers changes from 50 to 20 nm. Density functional theory-based calculations were carried out for the geometries of the CuO($\bar{1}$11)/Cu$_2$O(111) and TiO$_2$(111)/CuO($\bar{1}$11)/Cu$_2$O(111) heterostructures and their sensing mechanism toward alcohols of different chain lengths and molecular hydrogen. The reconstructed hexagonal Cu$_2$O(111) surface and the reconstructed monoclinic CuO($\bar{1}$11) and TiO$_2$(111) facets, all of which terminate in an O layer, lead to the lowest surface energies for each isolated material. We studied the formation of the binary and ternary heteroepitaxial interfaces for the surface planes with the best-matching lattices. Despite the impact of the Cu$_2$O(111) substrate in lowering the atomic charges of the CuO($\bar{1}$11) adlayer in the binary sensor, we found that it is the different surface structures of the CuO($\bar{1}$11)/Cu$_2$O(111) and TiO$_2$(111)/CuO($\bar{1}$11)/Cu$_2$O(111) devices that are fundamental in driving the change in the sensitivity response observed experimentally. The experimental data, supported by the computational results, are important in understanding the use of the multi-nanolayered films tested in this work as reliable, accurate, and selective sensor structures for the tracking of gases at low concentrations.
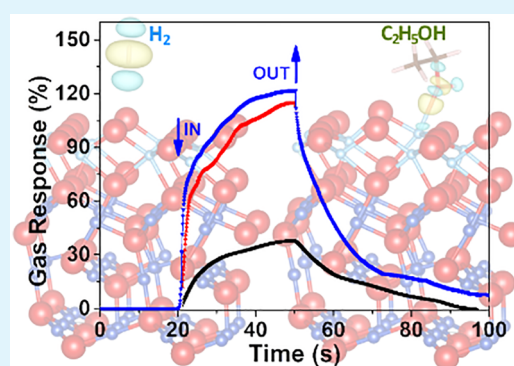
KEYWORDS: nanolayers, nanomaterials, multilayered films, CuO, p-type, Cu$_2$O, TiO$_2$, sensor

1. INTRODUCTION

Functional nanomaterials, including semiconducting oxide heterostructures with tunable performances, are an essential part of powered-semiconductor devices. However, synthesizing such nanocomposites has to be highly specific with respect to phase control at the nanoscopic level. Heterojunctions between different semiconducting oxide nanocrystals, especially those based on ultrathin films with mixed phases, improve the gas sensing properties with respect to the isolated phases due to their unique detection mechanism.[1−4] The specific features of the heterojunctions in nanocrystalline multilayered composites are crucial to control their gas sensing characteristics, i.e., the selectivity and gas response of the sensor, as a result of the exposed surface and interface phenomena.[1,5,6] A seminal work

by Brattain and Bardeen[7] reported that gas adsorption on semiconducting surfaces produces a change in their electrical conductance,[7] which has contributed to the further development of the sensor industry based on solid state materials.

From the nanotechnology point of view, metallic copper (Cu) and its oxides have received much attention due to their variety
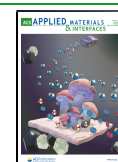
of real applications, particularly in the field of new nano-technology components for microelectronics.[4,8,9] Copper oxides are p-type semiconducting oxides and can be obtained in forms such as cuprite (Cu_2O) and cupric oxide (CuO) depending on the oxygen availability. The cuprous oxide cuprite (Cu_2O) is among the earliest semiconducting oxides used in solid-state electronics.[6,10,11] Although cuprite has been the focus of numerous experimental and theoretical studies[1,7,12−14] aimed at understanding its vibrational and optical properties, the electronic properties of Cu_2O continue to puzzle the scientific community. As applications of Cu_2O in nanoelectronics, photovoltaics, solid-state electronics, biosensing, and spin-tronics emerge,[4,9,15] including the light-driven purification of wastewater,[8] understanding the electronic structure of Cu_2O at the atomic level is important for the control of its properties and the identification of future applications in devices or nano-devices.

CuO has a band gap in the range of 1.2−2.1 eV and p-type semiconducting properties[12] that offer a significant advantage for sensing applications, especially in mixed CuO/Cu_2O phases.[6,11] A summary of gas sensor structures based on copper oxide nanomaterials can be found in several reviews.[16−20]

The (111) surface has been found, both in simulations[13,21] and experimentally,[22] to be the most stable cuprite (Cu_2O) plane under a range of different conditions. Furthermore, the almost complementary ($\bar{1}11$) facet was observed to be highly prominent in the crystals of the more oxidized tenorite (CuO) phase.[23] Although less stable than other planes, the anatase $TiO_2(111)$ surface has been reported as one of the most reactive for photocatalytic applications[24] and H_2 evolution.[25]

Inorganic ultraviolet (UV) absorbers such as titania (TiO_2), ZnO, and CeO_2 are generally employed in shielding applications for the UV protection of different surfaces,[26,27] where effective physical nanocoating barriers are needed for high-temperature applications.[28] Titania (TiO_2) nanocoatings are used extensively to increase the surface hardness and adhesive strength, provide long-term and high-temperature protection against corrosion, enhance tribological properties, and improve the design of the transparent coatings for self-cleaning surfaces.[27−30]

The detection and discrimination of volatile organic compounds (VOCs), which are classified as hazard vapors with adverse short- and long-term consequences on the environment and human health,[31] are important in the continuous monitoring of indoor air quality and therefore require reliable sensors. Moreover, exhaled VOCs can serve as biomarkers to assist in the noninvasive identification of various diseases. For example, acetone indicates diabetes[14,32−35] and isoprene, toluene, and acetic acid are signals of lung cancer,[31,36−38] making breath testing a highly promising approach for noninvasive cancer screening.[39] VOC analysis in patient breath offers insights into the anatomical and physiological metabolic processes that are altered by underlying diseases,[40,41] although a detailed mechanistic pathway of the metabolic routes leading to these molecules is still under investigation.[39]

This study reports the fabrication of stable ethanol sensors using multi-nanolayered films consisting of titania/cuprite/cupric oxide ($TiO_2/CuO/Cu_2O$/glass). The cuprite/cupric oxide structures are produced by a method based on sputtering combined with thermal annealing, before titania is sprayed on the surface of the CuO/Cu_2O/glass substrate. Interdigitated Au electrodes are deposited on the top surface of the specimens to connect the heterostructures and perform the gas sensing tests.

The morphology, composition, and the structural, electrical transport, and gas sensing properties of the materials are also studied. Moreover, a theoretical analysis based on density functional theory (DFT) calculations of the binary hetero-junction $CuO(\bar{1}11)/Cu_2O(111)$ and the ternary heterostructure $TiO_2(111)/CuO(\bar{1}11)/Cu_2O(111)$ have been carried out. First, we investigated the structures and relative stabilities of the hexagonal and monoclinic surfaces for each isolated material before elucidating the arrangement of the heteroepitaxial junctions and reporting their work function values and scanning tunnelling microscopy (STM) images. The calculated values of the work function rationalize the reactivity trends of the binary and ternary heterojunctions, whereas their computed STM images compare well with the experimental SEM images. The adsorption energies were computed for molecular hydrogen (H_2), ethanol (C_2H_5OH), and n-butanol (n-C_4H_9OH), and we plotted the electron charge density flow after the interaction with the heterojunctions in order to interrogate their selectivity changes.

2. EXPERIMENTAL SECTION

Glass slides from Thermo Scientific (2.5 × 7.5 cm) were employed as the substrates for the development of the devices. The glass substrates were cleaned by dipping them in HCl (11%) and then rinsed with distilled H_2O and acetone for 11 min, followed by an ultrasonic bath in ethanol for 11 min and rinsing in deionized H_2O.[1,42] Afterward, the CuO/Cu_2O ultrathin layers with thicknesses of 20, 30, 40, 50, and 60 nm were prepared on top of the clean glass by sputtering metallic copper under vacuum conditions. The Cu sputtering was carried out using a custom-built RF-magnetron system at 25 °C, a pressure of 3.6 × 10^{-3} mbar, an argon gas flux of 22 sccm, and a power of 51 W. Evochem GmbH, Germany supplied the copper metal with a high purity of 99.999% and a radius of 2.5 cm. The deposition rate of 6 nm min^{-1} was determined experimentally using a profilometer. Then, the metallic copper layers deposited on the glass substrates were thermally treated at 420 °C under normal atmospheric conditions for 30 or 60 min. The temperature for the thermal treatment was in accordance with our previous work on the ultrathin mixed CuO-Cu_2O oxide film.[6,43] Five different sample sets were produced with thicknesses of 20, 30, 40, 50, and 60 nm for the CuO/Cu_2O layer on the microscopic glass substrate. Next, titania (TiO_2) films were spray pyrolysis-deposited on top of the mixed copper oxide phase layers to prepare another five sample sets. Afterward, all materials were mounted on a thermal heating plate, which was kept at a temperature at 420 °C for 25 min prior to starting the spray pyrolysis process, as published previously by Pauporté et al.[27,42,44] For the spray pyrolysis, the precursor was delivered as a mixture of 7.1 mL of isopropanol, 0.62 mL of titanium(IV) tetra-isopropoxide (TTIP), and 0.41 mL of acetylacetone. The carrier gas used, which was selected as previously reported,[42,44] was an oxygen flow in order to blow the mixed aerosol through a valve with a diameter of 10 mm directly onto the surface of CuO/Cu_2O/glass composite, which remained on the heated hot plate at 420 °C for the entire spray process. The CuO/Cu_2O samples were grown with different thicknesses of 20, 30, 40, 50, and 60 nm and labeled as Cu20, Cu30, Cu40, Cu50 and Cu60, respectively. Afterward, the $TiO_2/CuO/Cu_2O$ heterostructures were treated under air at 420 °C for another 30 min (Cu20, Cu30, and Cu40) or 60 min (Cu50 and Cu60), depending on their thickness, then allowed to cool spontaneously. The thickness of the TiO_2 layer was monitored throughout the volume of the spray solution, as reported previously.[42,44]

After the preparation of the materials, Au electrodes were grown on top of the nanolayered $TiO_2/CuO/Cu_2O$ samples through an Al meander-shaped mask.[6,43] The Au top contacts had a thickness of ∼180 nm and a separation of 1 mm between the interdigitated electrodes. The Au target (purity of 99.99% and radius of 2.5 cm), which was produced by Evochem GmbH, Germany, was mounted on the magnetron (DC). The chamber pressure during Au sputtering was 3.55 × 10^{-3} mbar, the
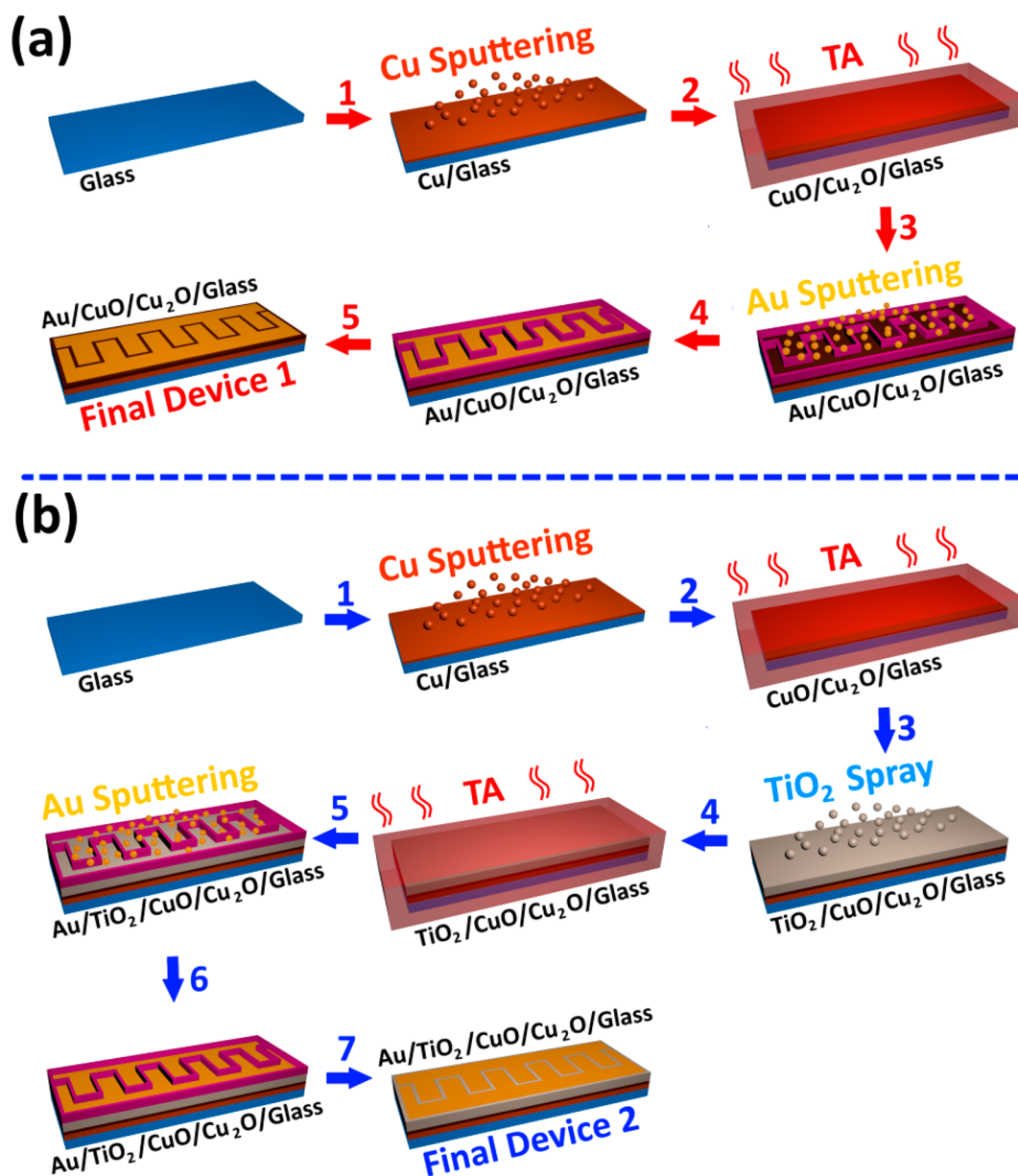
Figure 1. Technological flowchart for the manufacture of the (a) CuO/Cu$_2$O (final device #1) and (b) TiO$_2$/CuO/Cu$_2$O (final device set #2) nanostructured layered films sensor devices.

flow rate of Ar was about 16 sccm, and the sputtering power was set at 51 W, enabling a deposition rate of about 47 nm min^{-1}.[42] The morphological, structural, chemical, and micro-Raman (MR) measurements as well as X-ray photoelectron spectroscopy (XPS) investigations were carried out as published previously.[1,45] MR experiments were done using a Raman WITec Alpha300 RA spectrometer at 22 °C, as reported previously.[46] Graphite monochromatized Cu Kα radiation (1.5405 Å) at 40 kV and 40 mA was used for the X−ray diffraction (XRD) experiments, which were carried out using a Seifert 3000 TT instrument.[33] X-ray photoelectron spectroscopy (XPS) was used to measure the thickness of the TiO$_2$/CuO thin films via an Omicron Nano-Technology GmbH, Al anode, P = 240 W, as reported previously.[42] We charge calibrated the spectra with respect to the signal at 284.5 eV, corresponding to the aliphatic carbon C-1s, using the "CasaXPS" software ver. 2.3.16. We employed a Varian Cary 5000 spectrophotometer to carry out the characterization of the optical properties of the samples, where we used the integrating sphere supplied in the wavelength values between 300 and 2500 nm as described previously.[47] The gas detection characteristics were obtained using the setup and protocol described previously[6,43,48,49] at 30%

relative humidity (RH). A computer-controlled Keithley 2400 sourcemeter at a 0.25 V applied bias voltage was used to continuously record the electrical measurements, which were processed through the LabView software (from National Instruments). The responses to gas and VOCs were defined as the ratio $\left(\frac{R_g - R_a}{R_a} \cdot 100\% \right)$, where R_g and R_a are the electrical resistances of the specimens exposed to the gas or VOC and air under normal environmental conditions, respectively.[6,43]

The surface properties of the binary and ternary heteroepitaxial interfaces were simulated using unrestricted density functional theory (DFT) simulations, which are described in Text S1 (Supporting Information).

Figure 1 shows the technological flow for the manufacture of the mixed-phase (a) CuO/Cu$_2$O (final device set #1) and (b) TiO$_2$/CuO/Cu$_2$O (final device set #2) nanofilm devices. The general process can be described as follows: step 1, a precleaned glass substrate is sputtered with copper nanoparticles with a radius of about 2−5 nm to obtain ultrathin films of copper with thicknesses between 20 and 60 nm. Step 2, samples were thermally annealed in a furnace at a temperature of 420 °C for either 30 min (for sample sets Cu20, Cu30, and Cu40) or 60 min
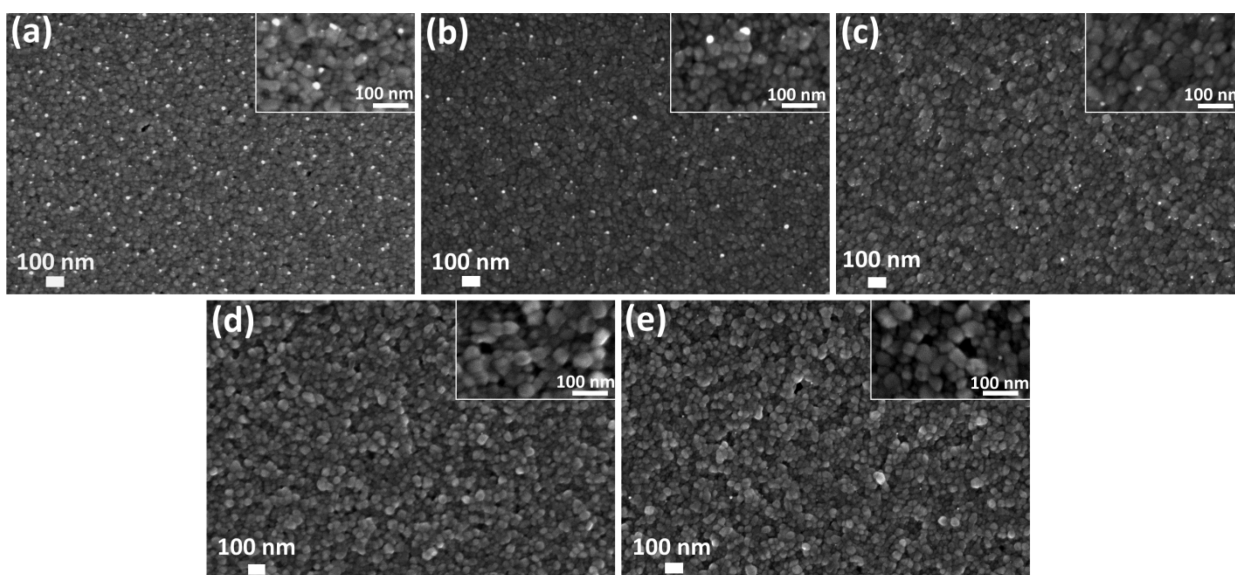
Figure 2. SEM images at (a) 20, (b) 30, (c) 40, (d) 50, and (e) 60 nm of the nanocrystallite CuO/Cu_2O samples that were grown using the sputtering—annealing approach and were thermally treated at 420 °C for 30 min. The inset shows a higher magnification of the SEM images.

(for sample sets Cu50 and Cu60) in air to develop the CuO/Cu_2O nanolayer heterojunctions. Steps 3 and 4 in Figure 1a are the deposition of the Au contacts by shading a metallic meander mask with a 1 mm gap. In step 5, we obtain device set #1 based on the CuO/Cu_2O nanolayers. Following steps 3 and 4 in Figure 1b, where the thin films of TiO_2 are deposited with a thickness of 20 nm and then thermally treated in a furnace at a temperature of 420 °C for either 30 min (for sample sets Cu20, Cu30, and Cu40) or 60 min (for sample sets Cu50 and Cu60) in air, we obtained the sensitive multi-nanolayered $TiO_2/CuO/Cu_2O$ heterojunction film. Steps 5 and 6 in Figure 1b are the deposition of the Au contacts as in Figure 1a. Finally, step 7 represents the final device set #2, i.e., the $TiO_2/CuO/Cu_2O$ heterostructure. It is important to mention that the layers are drawn as straight lines in Figure S1 but in reality are rough polycrystalline layers (Figure 2). Figure S1 displays the cross-section view of the devices from device set #1, which is made of CuO/Cu_2O nanolayers (device 1), and device set #2, which is based on heterolayers of $TiO_2/CuO/Cu_2O$ heterolayer films (device 2).

3. RESULTS AND DISCUSSION

3.1. Morphology and Composition Analyses. The insets of Figure 2a–f present the low- and high-magnification SEM images of the nanocrystallite CuO/Cu_2O samples, which were grown using a reproducible spraying—sputtering—annealing approach due to the possibility of controlling the speed of the sputtering growth. Thus, we simultaneously obtained five sample sets from a single substrate before thermally annealing them at 420 °C for either 30 min (for sample sets Cu20, Cu30, and Cu40) or 60 min (for sample sets Cu50 and Cu60) in air. It can be clearly observed that the volume of the nanoparticles essentially changes with the film thickness, which also affects the sensing properties. For the CuO nanoparticles, their larger electrical conductivity leads to some bright dots in the areas exposed to the electron beam of the SEM, which can be seen in Figure 2a–c[43]. The nanoparticles, which appear much smaller in size in the SEM images due to the thinner films, oxidize completely during the 30 min of annealing time. The ultrathin films possess very good adhesion to the microscopic glass substrates, as we have not seen signs of delamination during the three years that we have been investigating these types of samples.[1,12]

3.2. X-ray Photoelectron Spectroscopy and Micro-Raman Characterization. For the $TiO_2/CuO/Cu_2O$-layered thin-film sensor, the X-ray photoelectron spectra (XPS) are presented in Figure 3, where the overview spectrum shown in Figure 3a attests to the presence of the Cu, O, Ti, Na, and C elements. Cu, O, and Ti originate from the TiO_2/CuO layers, whereas the signal from carbon is as reported previously.[1,48] The
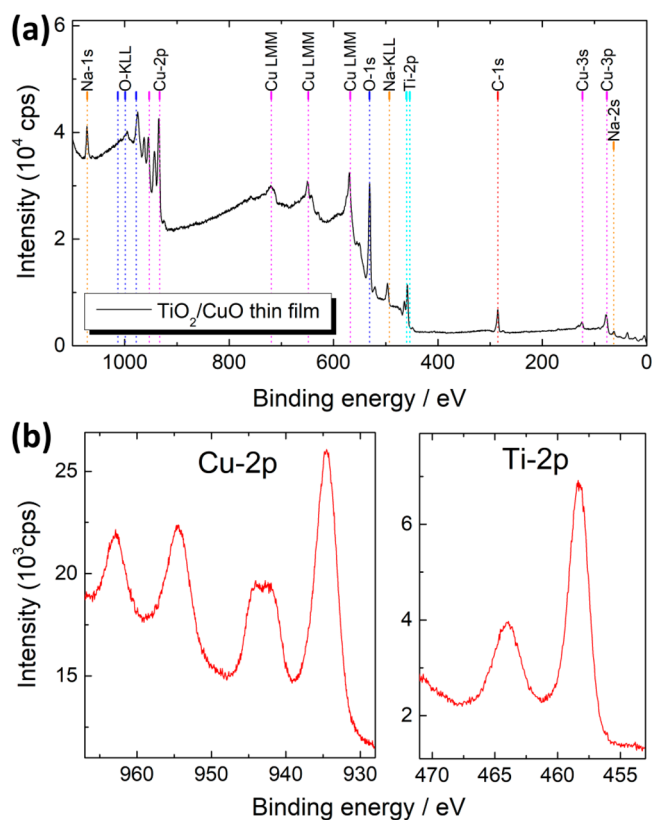

Figure 3. XPS of a TiO_2—CuO (red line) thin film sensor, show (a) an overview spectrum (b) high-resolution spectra of the Cu-2p and Ti-2p lines.
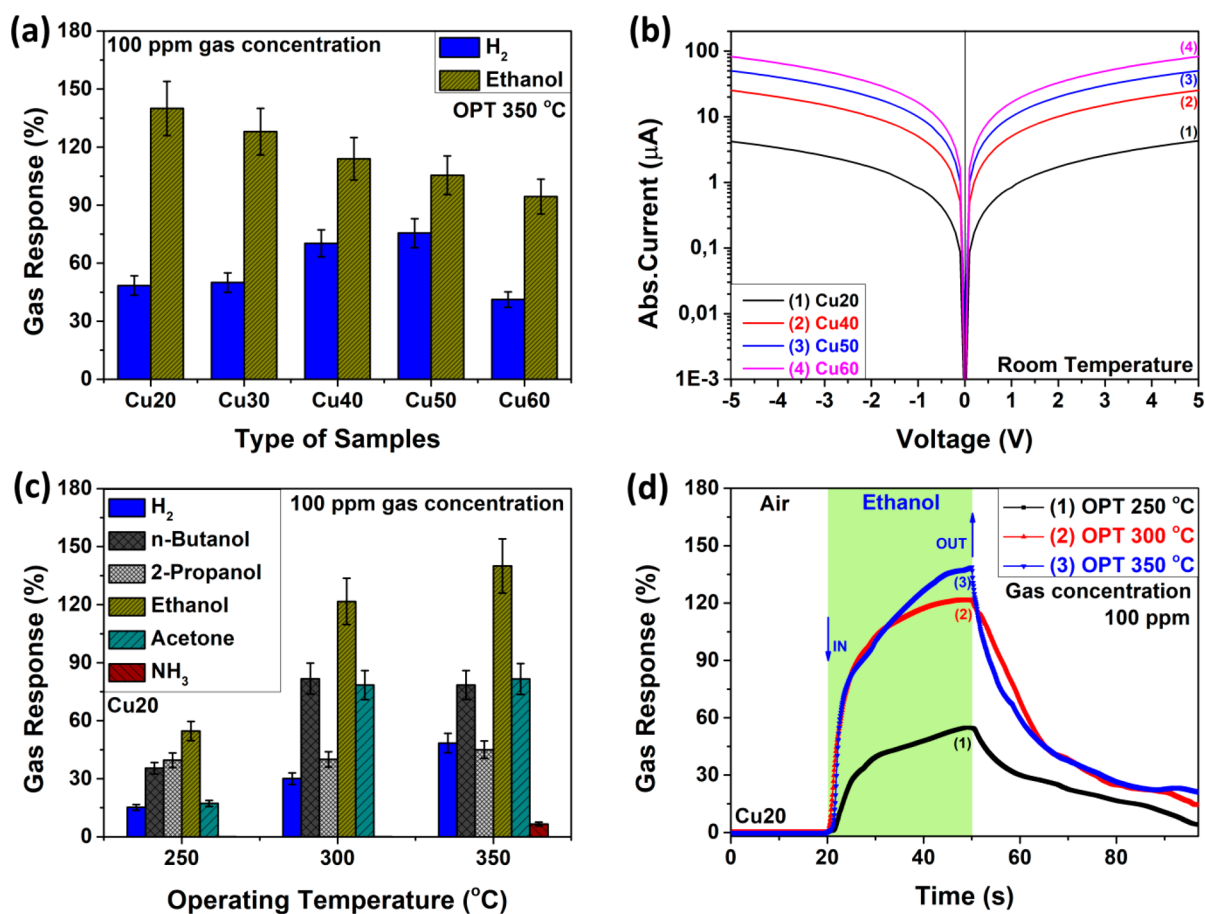
Figure 4. (a) Hydrogen and ethanol response of the CuO/Cu$_2$O samples with different thicknesses of 20 (Cu20), 30 (Cu30), 40 (Cu40), 50 (Cu50), and 60 nm (Cu60) at an operating temperature of 350 °C. (b) The $I-V$ current−voltage characteristics of the CuO/Cu$_2$O Cu20, Cu40, Cu50, and Cu60 samples, which were measured at room temperature. (c) Response to different gases (hydrogen, n-butanol, 2-propanol, ethanol, acetone, and ammonia) versus the operating temperature of the CuO/Cu$_2$O Cu20 samples. (d) Dynamic response of the CuO/Cu$_2$O Cu20 sample to ethanol.

Na peak corresponds to the glass substrates[42] used for the deposition of the sensor structures, which were cut for the XPS experiments.

High-resolution Cu-2p and Ti-2p lines are depicted in Figure 3b. A closer look at the Cu-2p line reveals clear Cu-2p$_{1/2}$ and Cu-2p$_{3/2}$ satellite lines, which are shifted to higher binding energies. The observed satellite peaks in the spectrum are commonly regarded as signatures for the presence of CuO,[43,50] which is found in the base layer of our samples.

The signals between 459.6−458.0 eV are due to Ti-2p$_{3/2}$, which is usually assigned to Ti in TiO$_2$. The evaluation of the high-resolution Ti-2p XPS spectra reveals that the line at 458.3 eV corresponds to Ti-2p$_{3/2}$. The separation of 5.6 eV between the Ti-2p$_{3/2}$ and Ti-2p$_{1/2}$ peaks and the position of the Ti-2p$_{3/2}$ signal illustrate the presence of Ti as TiO$_2$ in the base layer, according to the literature.[51,52]

The Raman scattering method is a useful spectroscopic technique to measure the vibrational modes and phase of ultrathin layers, heterostructures, and nanomaterials.[11,45] Micro-Raman spectroscopy was employed to investigate the characteristics at the nanoscale, namely, the lattice dynamics (electron−phonon interaction) of the CuO/Cu$_2$O and TiO$_2$/CuO/Cu$_2$O nanomaterials. The micro-Raman spectra in the range 100−1000 cm^{-1} were obtained at room temperature for the CuO/Cu$_2$O and TiO$_2$/CuO/Cu$_2$O nanomaterials, as shown in Figures S2 and S3.

The Raman studies clearly indicate the formation of the mixed copper oxide phases, namely CuO/Cu$_2$O, following thermal annealing at 420 °C under ambient conditions as well as the TiO$_2$/CuO/Cu$_2$O heterostructure after spraying a TiO$_2$ nanolayer on top of the binary films, which show the existence of heterostructured mixed-phase films. A detailed description of the aforementioned results is given in Text S2 (Supporting Information).

3.3. Ultraviolet, Visible, and Near-Infrared spectroscopy. Ultraviolet, visible, and near-infrared (UV−vis-NIR) absorption spectroscopy is a characterization method used to study the energy level and optical properties of transparent semiconducting oxide materials. The room temperature spectra of the CuO/Cu$_2$O and TiO$_2$/CuO/Cu$_2$O heterostructures allowed the detection of the optical absorption and excitonic transitions characteristic of the nanolayers. The transmission and absorption spectra are presented in Figure S4, and the plots of $(\alpha h\nu)^2$ versus the photon energy ($h\nu$) for the CuO/Cu$_2$O and TiO$_2$/CuO/Cu$_2$O heterostructures are shown in Figures S5 and S6. More details of the UV−vis-NIR characterization are provided in Text S3 (Supporting Information).

3.4. Gas Sensing Properties. First, we will focus on the CuO/Cu$_2$O samples and their gas sensing performances. Then, we will discuss the gas sensing performances of the TiO$_2$/CuO/Cu$_2$O nanolayered materials, which we will compare to those of the base layer.
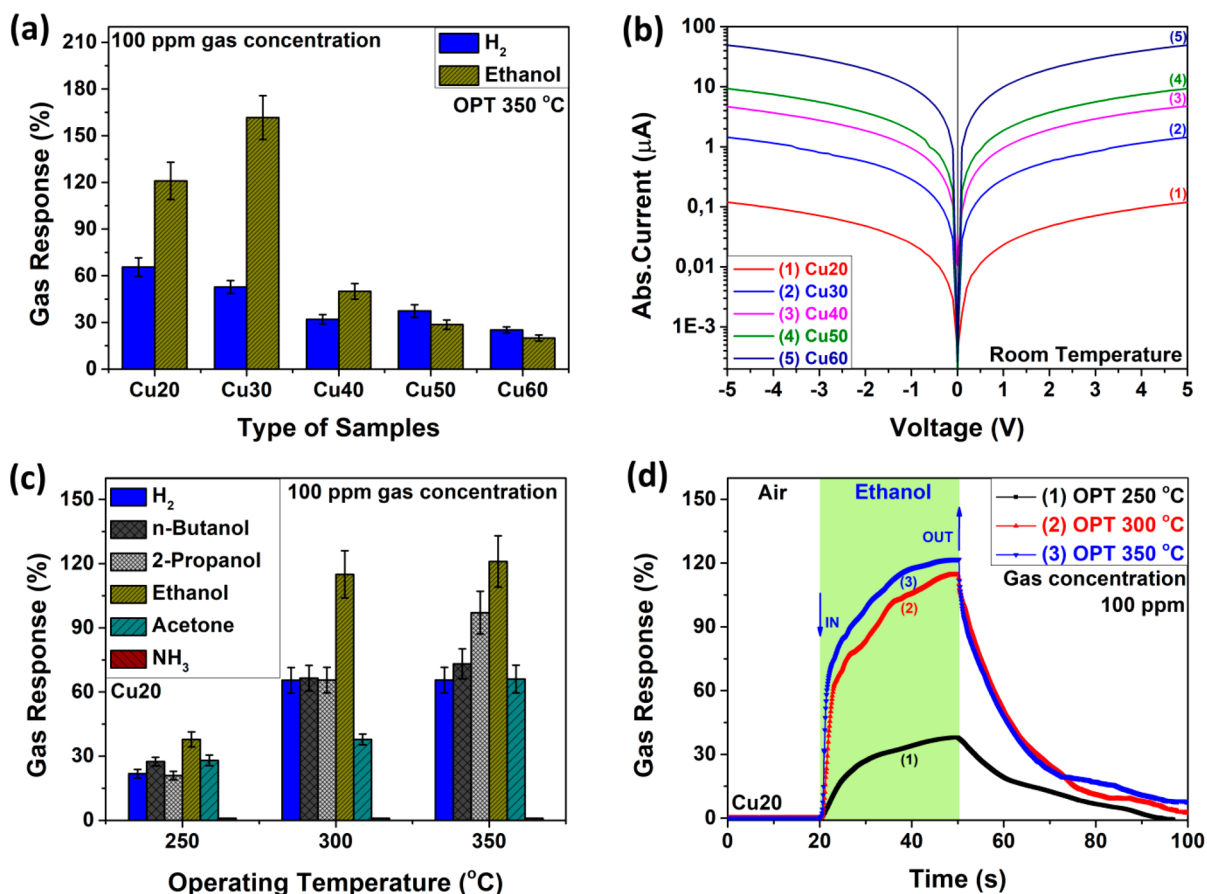
Figure 5. (a) Hydrogen and ethanol responses of the TiO$_2$/CuO/Cu$_2$O samples with different thicknesses of 20 (Cu20), 30 (Cu30), 40 (Cu40), 50 (Cu50), and 60 nm (Cu60), which were measured at 350 °C. (b) Current–voltage characteristic at room temperature. (c) Response to different compounds (hydrogen, *n*-butanol, 2-propanol, ethanol, acetone, and ammonia) versus the operating temperature of the TiO$_2$/CuO/Cu$_2$O Cu20 sample. (d) Dynamic response of the TiO$_2$/CuO/Cu$_2$O Cu20 sample to ethanol.

Gas Sensing Results of CuO/Cu$_2$O. The CuO/Cu$_2$O-based Cu20, Cu30, Cu40, Cu50, and Cu60 nanolayer samples were connected in the sensor structures, as indicated schematically in Figure S1.

Figure 4a represents the responses to hydrogen and ethanol at the standard deviations between multiple measurements of the CuO/Cu$_2$O samples at an operating temperature of 350 °C, from which it is clear that the Cu20 and Cu30 samples show the highest response to ethanol. From Figure 4a, we observe that, for all thicknesses, the CuO/Cu$_2$O specimens are more selective to ethanol compared to the other tested gases (hydrogen, ethanol, 2-propanol, *n*-butanol, acetone, and ammonia). However, the response, selectivity, and electrical resistance of the sensors decrease as the thickness of the layers increases (more than 30–40 nm), which is in accordance with previously reported data.[6] The optimum thickness is therefore in the range of 20–30 nm (sample sets Cu20 and Cu30). The response values of CuO/Cu$_2$O nanolayers to different analytes depend on their thickness, specifically when it is in the order of the Debye length.[43,53] The sensing mechanism proposed for these results for the binary heterostructure is explained in Text S4 (Supporting Information).

Figure 4b represents the current–voltage (*I*−*V*) curves of the prepared structures, and it can be seen from Figure S7a that the plots are linear at room temperature for all samples. According to the data in Figure 4b and Figure S7a, the *I*−*V* plots for all the CuO/Cu$_2$O samples of different thicknesses show an Ohmic

contact behavior between the CuO/Cu$_2$O nanolayers and the Au top contact at room temperature. However, at the operating temperature of 350 °C (Figure S8a), the current−voltage characteristics are nonlinear and can be attributed to a conductivity effect driven by the energy barrier. The variation of the electrical current with temperature (see Figure 4c) indicates that the heterostructure is also convenient for temperature measurement. We used eq 1 to express the electrical resistivity of our *p*-type semiconducting oxides as follows:[54]

$$\rho \equiv \frac{1}{\sigma} = \frac{1}{q\mu_p p} = \frac{1}{q\mu_p\left(N_V e^{[-(\frac{E_F-E_V}{KT})]}\right)} = \frac{e^{(E_F-E_V/KT)}}{\sigma\mu_p N_V} \tag{1}$$

where ρ is the electrical resistivity, σ is the electrical conductivity, q is the charge of the electron, μ_p is the mobility of the holes, p is the concentration of the holes, N_V is the concentration of the acceptors, E_F is the Fermi energy, E_V is the maximum energy of the valence band, T is the absolute temperature, and k is the Boltzmann constant.

The response variation of the structures to 100 ppm of ethanol as a function of the operating temperature was studied to find the optimal working conditions. Figure 4c shows the response of Cu20 (CuO/Cu$_2$O sample) to different gas molecules (hydrogen, *n*-butanol, 2-propanol, ethanol, acetone, and ammonia) at operating temperatures between 250 and 350 °C. The standard deviation between multiple measurements of the same sample
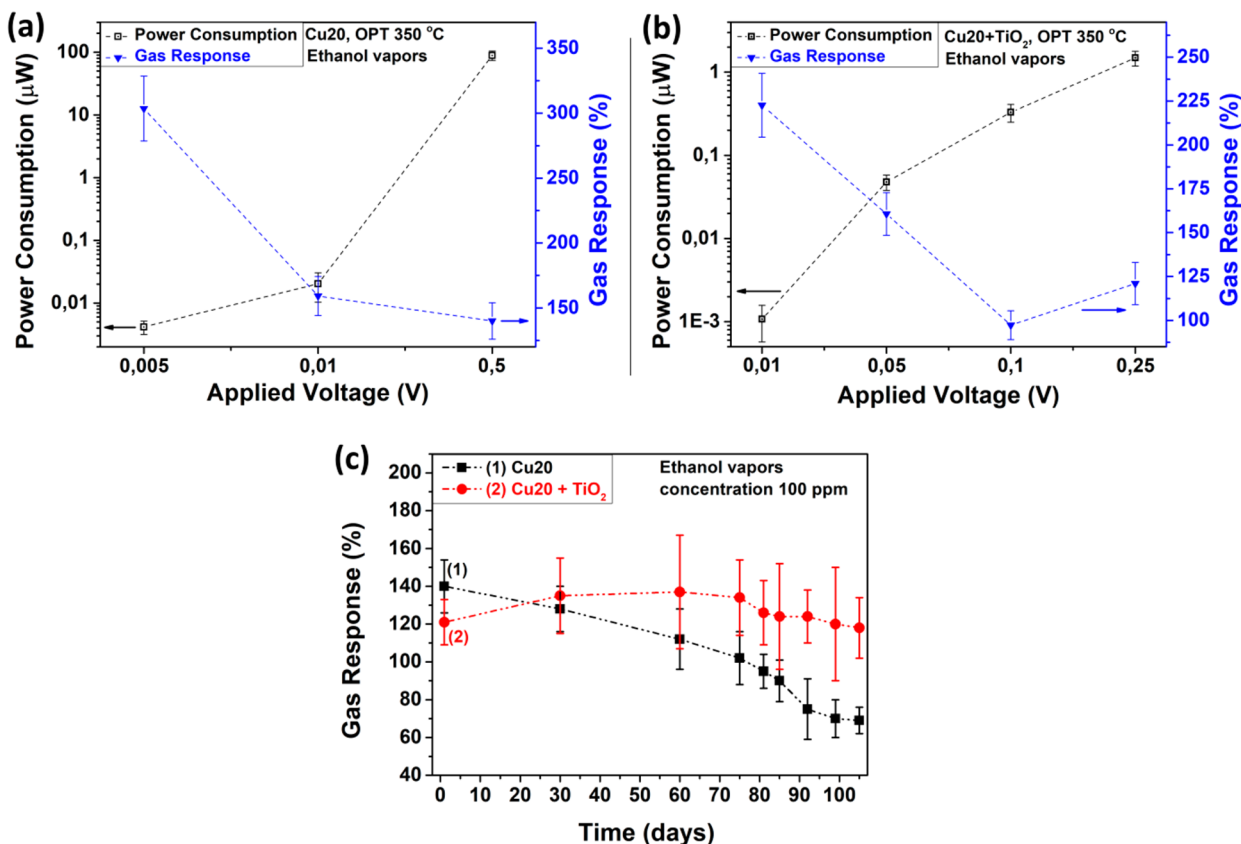
Figure 6. Dependence of the power consumption and the gas response with respect to the applied voltage for the (a) CuO/CuO$_2$ and (b) TiO$_2$/CuO/CuO$_2$ samples with a thickness of 20 nm (Cu20). (c) Variation of the gas response to ethanol vapors over time for the CuO/CuO$_2$ and TiO$_2$/CuO/CuO$_2$ samples with a thickness of 20 nm (Cu20).

set is indicated with error bars. For ethanol vapors, the response of the sensor at 350 °C is larger compared to those for the other gases. Sample sets tested at 250, 300, and 350 °C have the highest response to ethanol with values of ∼24%, ∼121%, and ∼140%, respectively, whereas Figure 4c also shows that the hydrogen response improved with the operating temperature. The sensing response of the CuO/Cu$_2$O heterostructure with a thickness of between 20 and 30 nm demonstrates the *p*-type behavior of this material. The operating-temperature dependence of the response variation of the structure to 100 ppm of ethanol was investigated to find the optimal working conditions, Figure 4d indicates the dynamic response of the Cu20 sample to 100 ppm of ethanol. We observe that the response time (t_r) and the recovery time (t_d) are relatively small under the operating temperatures of 250, 300, and 350 °C (t_r = 18.8, 13, and 18.5 s, respectively, and t_d = 43.3, 46.4, and 49.6 s, respectively). Then, we prepared more complex structures based on TiO$_2$/CuO/Cu$_2$O and studied their sensing properties toward H$_2$ and ethanol, allowing us to explain the effect of each layer in detail.

Gas Sensing Performances of TiO$_2$/CuO/Cu$_2$O. The hydrogen and ethanol responses of the samples consisting of the TiO$_2$/Cu$_2$O/CuO multi-nanolayered films with different thicknesses were studied to determine the impact of adding TiO$_2$ to the top layer. The ternary heterojunction can also act either as a self-cleaning surface or to enhance the gas detection and improve the protection against corrosion at high temperatures.[27−30,55,56]

Figure 5a shows the responses of the TiO$_2$/CuO/Cu$_2$O Cu20, Cu30, Cu40, Cu50, and Cu60 samples to hydrogen and ethanol, measured at the operating temperature of 350 °C. From

Figure 5a, we can see that the TiO$_2$/CuO/Cu$_2$O Cu20 and Cu30 samples are more sensitive toward ethanol than hydrogen gas. However, increasing the thickness of CuO/Cu$_2$O to Cu50 and Cu60 changes the sensing performance of the TiO$_2$/CuO/Cu$_2$O structures, and hydrogen becomes the most sensitive gas. However, the response values of sensors with the thicker layers of CuO/Cu$_2$O are lower toward hydrogen and ethanol compared to those of the Cu20 and Cu30 samples. The best sensing performances to ethanol were obtained for the samples with a thickness of 30 nm (sample Cu30). Figure 5b illustrates the electrical current−voltage plot of the TiO$_2$/CuO/Cu$_2$O samples, and the linear Ohmic behavior at room temperature can be seen in Figure S7b. However, as already stated, the *I-V* current−voltage plots are nonlinear at the operating temperature of 350 °C (Figure S8b) due to a conductivity effect driven by the energy barrier. Figure 5c presents the responses to different chemical compounds (hydrogen, ethanol, 2-propanol, *n*-butanol, acetone, and ammonia) versus the operating temperature of the TiO$_2$/CuO/Cu$_2$O Cu20 sample set. At all operating temperatures, i.e., 250, 300, and 350 °C, we see that the samples have the highest response to ethanol, with values of ∼38%, ∼115% and ∼121%, respectively. Comparatively (the data in Figure 4c and Figure 5c), the response value was enhanced with the increasing operating temperatures for the TiO$_2$/CuO/Cu$_2$O nanomaterial. Thus, there was no noticeable response for these sensor structures at operating temperatures below 250 °C due to surface reactions with different oxygen species. The maximum response was achieved at an operating temperature of 350 °C, which is the highest temperature allowed by our gas test equipment. Figure 5d indicates the dynamic
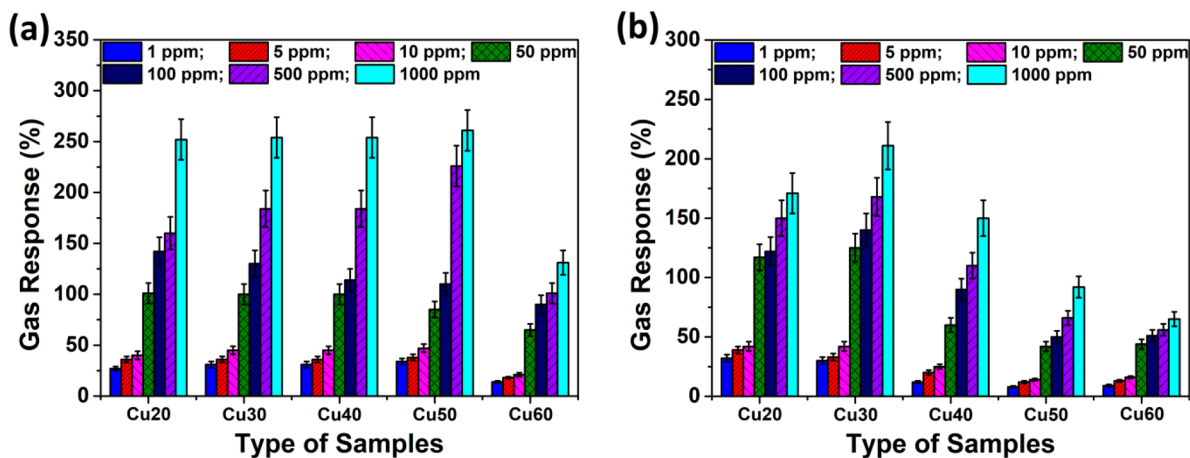
Figure 7. Gas response to various concentrations of ethanol vapor, measured at 350 °C, versus the type of sample for the (a) CuO/Cu$_2$O and (b) TiO$_2$/CuO/Cu$_2$O samples with different thicknesses of 20 (Cu20), 30 (Cu30), 40 (Cu40), 50 (Cu50), and 60 nm (Cu60).
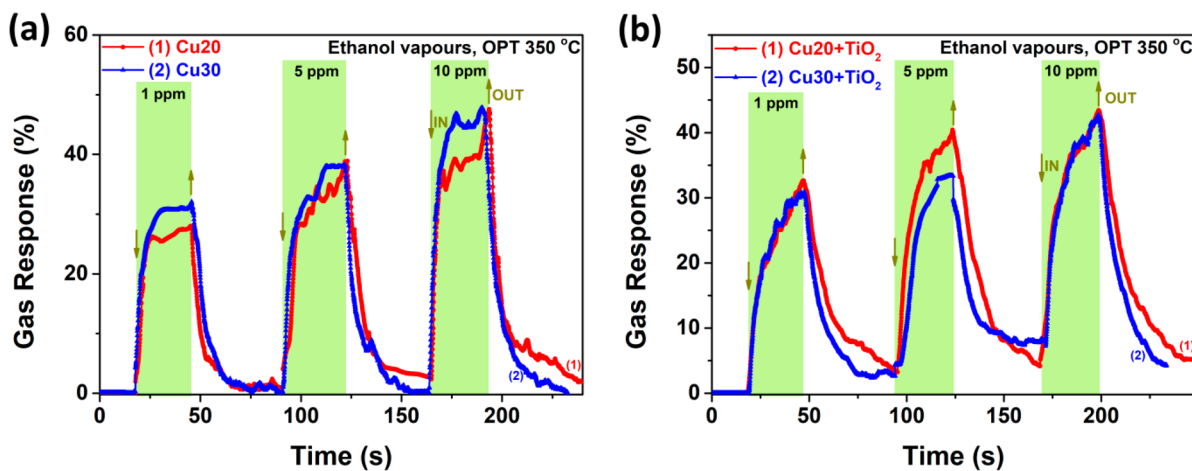

Figure 8. Dynamic response to 1, 5, and 10 ppm of ethanol vapor for the (a) CuO/Cu$_2$O and (b) TiO$_2$/CuO/Cu$_2$O samples with various thicknesses of 20 (Cu20) and 30 nm (Cu30).

response of the TiO$_2$/CuO/Cu$_2$O samples (prepared based on the Cu20) to 100 ppm of ethanol. For the working temperatures of 250, 300, and 350 °C, we observed that the response times (τ_r) were 18.9, 16.3, and 13.8 s, whereas recovery times (τ_d) were 35.5, 28.3, and 37.3 s, respectively, which are relatively low values.

Comparison of the Gas Sensing Features of Cu$_2$O/CuO and TiO$_2$/Cu$_2$O/CuO. Here, we compare the gas response of the multi-nanolayered Cu$_2$O/CuO and TiO$_2$/Cu$_2$O/CuO heterostructured films. Comparing the data in Figure 4c and Figure 5c indicates that the response to hydrogen increased for the ternary system with respect to the binary heterojunction at all operating temperatures. Figure 6a represents the relationship between the response to 100 ppm of ethanol vapors and the power consumption versus the applied voltage for the CuO/Cu$_2$O Cu20 samples. Figure 6a and b shows that when the applied bias voltage decreases, the response to the ethanol vapors increases, and the power consumption decreases, which can be attributed to the nonlinear $I-V$ current−voltage characteristics at an operating temperature of 350 °C (Figure S8a and S8b). For applied bias voltages of 0.5, 0.01, and 0.005 V, the power consumption is about 88, ∼0.02 and ∼0.004 μW (approximately 4 nW), and the response is about 140%, ∼160%, and ∼300%, respectively. This power consumption is part of the energy

consumption of the entire sensor, part of which is used to heat the sample to an operating temperature of 350 °C is not calculated here.

Figure 6b represents the response to 100 ppm of ethanol vapors and the dependence of the power consumption dependence on the applied bias voltage for the TiO$_2$/CuO/Cu$_2$O Cu20 sample set. This figure shows that when the applied voltage decreases, the power consumption also decreases. For example, the power consumption is about 1.5, ∼0.33, ∼0.05, and ∼0.001 μW (approximately 1 nW) at the applied voltages of 0.25, 0.1, 0.05, and 0.01 V, respectively. However, the gas response is ∼120% for the applied bias voltage of 0.25 V, which decreases to ∼97% under 0.1 V of an applied bias voltage and increases to ∼160% and ∼222% at applied bias voltages of 0.05 and 0.01 V, respectively.

Figure 6c represents the variation of the responses of the CuO/Cu$_2$O Cu20 (curve 1) and TiO$_2$/CuO/Cu$_2$O Cu20 (curve 2) samples to 100 ppm of ethanol vapor for 105 days. Figure 6c shows that the response to ethanol vapors decreases for the CuO/Cu$_2$O (curve 1) samples, whereas it remained unchanged in the case of the TiO$_2$/CuO/Cu$_2$O (curve 2) samples. Significant changes were not observed due to the self-cleaning effect of the ternary heterostructure.[55,56]
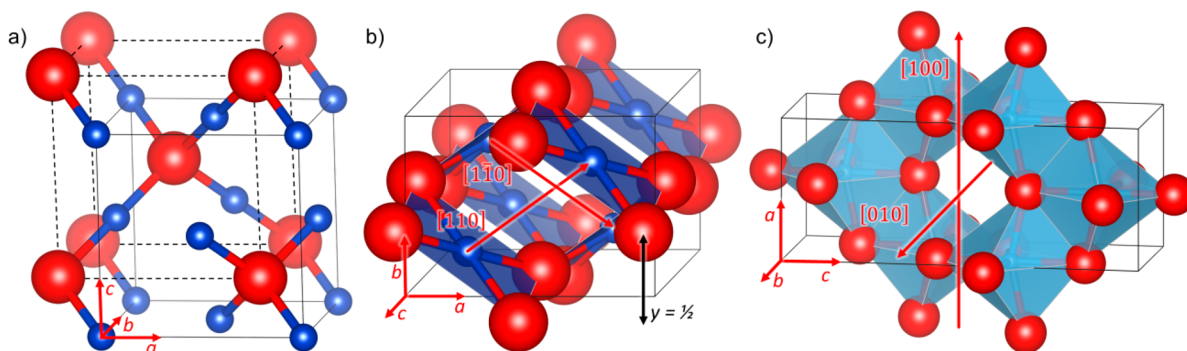
Figure 9. (a) Conventional cubic unit cell containing two formula units (f.u.) of cuprite Cu_2O. Solid lines represent the face-centered cubic (*fcc*) sublattice of Cu ions, and dashed lines indicate the body-centered cubic (*bcc*) sublattice of O atoms. (b) Conventional monoclinic unit cell containing 4 f.u. of tenorite CuO. The $^1_\infty[CuO_{4/2}]$ chains are shown along the $[110]$ and $[1\bar{1}0]$ directions, while the ideal staggering parameter *y* is represented in the direct coordinates. (c) Conventional tetragonal unit cell containing 4 f.u. of anatase TiO_2. The channels along the $[100]$ and $[010]$ directions are shown. Crystallographic directions are indicated for all structures. O atoms are shown in red, Cu atoms are shown in dark blue, and Ti atoms are shown in light blue. Polyhedral representations are used for the square planar Co atoms and the distorted octahedral Ti atoms.

According to the results presented in this study, changes in the conductance of the semiconductor oxide-based chemical sensors are caused by the interactions of environmental chemical compounds with the sensor surface, which are strongly influenced by the operating temperature.[2,57] An efficient way to improve the plots of the sensor is through controlling the catalytic properties of the oxide surface.[2,42]

Figure 7 shows the gas response to 1, 5, 10, 50, 100, 500, and 1000 ppm of ethanol versus the type of CuO/Cu_2O and $TiO_2/CuO/Cu_2O$ samples and their thicknesses (Cu20, Cu30, Cu40, Cu50 and Cu60); the responses were measured at the working temperature of 350 °C. Figure 7 suggests that all samples responded to all concentrations of ethanol.

Figure 8 shows the dynamic response of the CuO/Cu_2O (Figure 8a) and $TiO_2/CuO/Cu_2O$ (Figure 8b) samples with thicknesses of 20 (Cu20) and 30 nm (Cu30) to 1, 5, and 10 ppm of ethanol at 350 °C working temperatures. From the plot, it can be seen that the response of the sensors is relatively high at very low concentrations of ethanol. The sensing parameters of the CuO/Cu_2O and $TiO_2/CuO/Cu_2O$ samples with thicknesses of 20 (Cu20) and 30 nm (Cu30) to 1, 5, and 10 ppm of ethanol at an operating temperature of 350 °C are shown in Table S1. For the CuO/Cu_2O and $TiO_2/CuO/Cu_2O$ Cu20 and Cu30 samples, the dynamic response to 1 ppm of ethanol is shown in Figure S9.

The dynamic response by the CuO/Cu_2O and $TiO_2/CuO/Cu_2O$ Cu20 and Cu30 samples to various concentrations of ethanol (1, 5, 10, 50, 100, 500, and 1000 ppm) is shown in Figure S10. The gas response is presented in Figure S11, which shows the effect of different concentrations of hydrogen (100, 500, and 1000 ppm) versus the type and thickness of the CuO/Cu_2O and $TiO_2/CuO/Cu_2O$ Cu20, Cu30, Cu40, Cu50, and Cu60 sample sets measured at a 350 °C working temperature. Figure S11 displays that the response of the samples increases strongly at high concentrations of hydrogen.

Overall, the chemical detection mechanism proposed for CuO/Cu_2O relies on surface physicochemical reactions, which strongly depend on the operating temperature. More details of the gas detection mechanism are described in Text S4 (Supporting Information), and the energy band diagrams of heterostructures $TiO_2/CuO/Cu_2O$ in both air and ethanol vapors are represented in Figure S12.

3.5. Simulation of Bulk Phases. We first investigate the optimized bulk structures of the materials used to build the heteroepitaxial structures, which will later be used to simulate the molecular adsorption to compare with our experiments. Our starting point for the substrate is Cu_2O, which is characterized by the space group $Pn\bar{3}m$ (no. 224) and the cuprite structure with Cu in the lowest oxidation state of 1+.[58] Figure 9a presents the conventional cubic unit cell of Cu_2O with two formula units (f.u.). The O atoms are distributed in a body-centered cubic (*bcc*) sublattice, whereas the Cu ions are arranged in a face-centered cubic (*fcc*) sublattice. The twofold Cu atoms occupy the 4*b* Wyckoff linear positions with coordinates at the origin of the unit cell, while the fourfold O ions occupy the 2*a* tetrahedral crystallographic sites at (1/4, 1/4, 1/4). CuO, the material in the middle of the ternary heterostructure with Cu in the higher oxidation state of 2+, crystallizes in the tenorite structure with space group $C2/c$ (no. 15).[59] Figure 9b shows the conventional monoclinic unit cell of CuO with four f.u. In this structure, the fourfold Cu atoms are located at the 4*c* Wyckoff square planar positions with coordinates (1/4, 1/4, 0), whereas the fourfold O counterions fill the 4*e* distorted tetrahedral holes at (0, *y*, 1/4). CuO forms two sets of $^1_\infty[CuO_{4/2}]$ chains that are perfectly aligned along the $[110]$ and $[1\bar{1}0]$ directions.[60] The deviation of the *y* value from 1/2, in fractional coordinates, represents the staggering of the $^1_\infty[CuO_{4/2}]$ chains along the $[001]$ direction. The crystal structure of anatase TiO_2, the topmost material in the ternary heterojunctions, is tetragonal with space group $I4_1/amd$ (no. 141).[61] The conventional unit cell contains four f.u. of TiO_2, as depicted in Figure 9c. The distorted octahedral Ti^{2+} cations are in the 4*b* crystallographic positions with coordinates (0, 1/4, 3/8), and the O anions are in the 8*a* distorted trigonal planar sites at (0, 1/4, 1/6). The anatase TiO_2 structure displays channels in the $[100]$ and $[010]$ directions and dual chains of $^1_\infty[TiO_{6/2}]$ along the $[2, 2, 13]$ direction.

Table S2 shows the optimized and experimental lattice parameters for the cubic unit cell of Cu_2O, the monoclinic unit cell of CuO, and the tetragonal unit cell of TiO_2. Our calculations indicate that the lattice parameters were overestimated by 0.41% for CuO[59] and 1.59% for TiO_2,[61] while they were underestimated by 0.28% for Cu_2O.[58] The internal coordinates of the three materials were allowed to relax, with all ions showing a large preference for staying in their perfect Wyckoff crystallographic positions. The value calculated for

parameter y is 0.004 larger than that in the experiments, indicating that we can predict a smaller staggering for the $_\infty^1[CuO_{4/2}]$ chains along the $[001]$ direction in the simulated cell of CuO. The shapes of the conventional unit cells were fully optimized, but Cu_2O, CuO, and TiO_2 remained in the ideal cubic, monoclinic, and tetragonal structures, respectively. The perfect match between the simulated and experimental angle β further supports the undistorted monoclinic shape of CuO. More details and a description of the atomic Bader charges, atomic magnetic moments, and band gaps are provided in Text S5 (Supporting Information).

3.6. Simulation of Isolated Surfaces. We also simulated the pristine $Cu_2O(111)$ surfaces with a hexagonal symmetry and the $CuO(\bar{1}11)$ and $TiO_2(111)$ facets with a monoclinic symmetry, which were used to construct the binary and ternary heterojunctions, respectively. The surface slabs were constructed using METADISE[62] to cut the geometry optimized bulks. A vacuum gap of 20 Å was added above the surfaces to avoid spurious interactions between the periodic supercells. The two bottommost layers were kept at their relaxed atomic bulk positions to simulate the bulk phase, while the rest of the slab was allowed relax explicitly. We have applied dipole corrections in the direction perpendicular to the surface[63,64] to improve the description of the total energy of our single-surface models.[65−69] According to this formalism, a planar dipole sheet was introduced in the center of the vacuum region, and its strength was calculated self-consistently to compensate the artificial adsorbate-induced dipole.

The $Cu_2O(111)$ and $CuO(\bar{1}11)$ surface slabs have the smallest surface areas of 31.378 and 32.438 Å^2, respectively. The surface cell of Cu_2O contains 24 atoms, whereas that of CuO comprises 32 atoms distributed in four stacking sequences that consist of either 2 or 4 f.u.. The $TiO_2(111)$ surface was modeled using a slab with an area of 54.580 Å^2 and 36 atoms that occupied 12 stacking sequences of a single stoichiometric unit each. With this setup, we ensured that all surfaces were symmetric along the z-axis, and their widths were between 7.4 and 10.1 Å. The vacuum thickness and the total and relaxed number of surface layers were carefully tested until a convergence within 1 meV per atom was reached.

The stacking of the atomic layers is $(O)-(Cu_4)-(O)$ for the Cu_2O surfaces in the (111) direction, where the atoms within parentheses lie in approximately the same plane as that shown in Figure S13. Termination A is a type 2 Tasker surface,[70] with a top surface layer that has a bulk-like structure that terminates in threefold under-coordinated O atoms and 0.25 monolayers (MLs) of monocoordinated Cu atoms with a single dangling bond. Termination B is a reconstructed type 3 Tasker surface,[70] where the dipole moment was quenched by shifting half the monocoordinated Cu atoms from the topmost stoichiometric stacking sequence at the relaxed side of the slab to the unrelaxed side of the slab, which created twofold O anions. Following the relaxation of termination A, both the exposed threefold and subsurface fourfold O atoms moved outward by an average of 0.052 Å, while the cations migrated toward the bulk by only 42% of the displacement of the anions. We found that for termination B the displacement of the atomic layers is larger than for termination A. For the monocoordinated Cu atoms, 0.5 MLs shifted their position horizontally by 0.689 Å, with half of them even coordinating the twofold O atoms that only moved 0.141 Å toward the vacuum. This surface reconstruction and the atomic displacements effectively increased the coordination number of both the exposed O and Cu atoms for the relaxed termination B.

Despite their different crystal structures, the stacking of the atomic layers for CuO in the $(\bar{1}11)$ direction is similar to that for Cu_2O in the (111) direction except for their different stoichiometric ratios, as illustrated in Figure S14. Unsurprisingly, both terminations A and B of the $CuO(\bar{1}11)$ surface display many of the same characteristics as its $Cu_2O(111)$ counterpart. For example, termination A is a type 2 Tasker[70] surface that presents bulk-like structured threefold O and Cu atoms, of which the 0.5 MLs is threefold. Similar to the reduced copper oxide phase, the exposed atoms exhibit the lowest coordination numbers in termination B of $CuO(\bar{1}11)$, which is also a reconstructed type 3 Tasker surface.[70] Due to the surface construction, 0.5 MLs of the Cu atoms left exposed are twofold, whereas 0.25 MLs of the counteranions are twofold, 0.50 MLs are threefold, and the remaining keep the distorted tetrahedral configuration of the bulk. After relaxation, the exposed O atoms of both terminations moved outward by an average distance of ∼0.2 Å, whereas the cations shifted their locations horizontally by 0.164 Å toward the vacuum in termination A and 0.518 Å inward in termination B, where they also became threefold.

$TiO_2(111)$ is a type 2 Tasker surface[70] composed of thin $(O)-(Ti)-(O)$ planes with a width of 0.220 Å and a separation of 0.434 Å from the neighboring stoichiometric units, which explains why only one termination is possible for this facet, as displayed in Figure S15. Cutting the bulk of TiO_2 reduces the coordination number of the exposed atoms, i.e., 0.5 MLs of Ti become fourfold, whereas the other half are surrounded just by three O ions compared to the octahedral coordination environment in the bulk. Moreover, 0.75 MLs of the anions are twofold, and 0.25 MLs are monocoordinated in the freshly created surface. During relaxation, the least-coordinated Ti ions moved 0.235 Å inward. The fourfold Ti remained approximately at the same position, and the Ti of the third stoichiometric unit migrated 0.511 Å toward the surface, becoming completely penta-coordinated and appearing roughly at the same layer. Moreover, all the O atoms have a coordination number of two after surface relaxation, with the largest average inward displacement of 0.442 Å observed for the topmost stoichiometric unit. The anions of the third stoichiometric unit also experienced notable outward shifts of 0.708 Å.

We have calculated the surface energies before (γ_u) and after (γ_r) relaxation as

$$\gamma_u = \frac{E_u - n_{bulk} \cdot E_{bulk}}{2A} \tag{2}$$

$$\gamma_r = \frac{E_r - n \cdot E_{bulk}}{A} - \gamma_u \tag{3}$$

where n_{bulk} is the number of f.u. contained in the surface cell, E_u is the energy of the slab with all atoms at their optimized bulk positions, E_{bulk} is the energy of the bulk per f.u., E_r is the energy of the half-relaxed slab, and A is the surface area of one side of the slab. The degree of relaxation (R) was quantified as R = 100 × $(\gamma_u - \gamma_r)/\gamma_u$.

From our simulation of the surface energies, which are listed in Table S3, we determined that terminations A are the most stable for $Cu_2O(111)$ and $CuO(\bar{1}11)$ both before and after relaxation. The calculations also reveal that the overall most stable surface is $Cu_2O(111)$ with a relaxed surface energy of γ_r = 70 meV Å^2. $TiO_2(111)$ is the least thermodynamically stable plane in this study, since its surface energy is one order of magnitude larger than those for any other material. Despite their similar relaxed surface energies, termination A of $Cu_2O(111)$

only experiences a small degree of relaxation $R = 4.08\%$, while termination A of CuO($\bar{1}11$) suffers a relaxation approximately five times larger. Terminations B of both copper oxide surfaces have the largest degree of relaxation in agreement with the displacement of their respective atomic layers, while the TiO$_2$(111) facet shows a modest 9.69% degree of relaxation. The lower charges of the undercoordinated atoms suggest that all surfaces are less ionic than their respective bulks. Our calculations indicate that the increasing order of ionic character for the surfaces is Cu$_2$O(111) < CuO($\bar{1}11$) < TiO$_2$(111), which is in line with the trend found for the charges in their respective bulk phases. The surface atoms of both Cu$_2$O(111) and TiO$_2$(111) are nonmagnetic, as evidenced by their lack of magnetic moments. The exposed Cu atom in CuO experiences a reduction of its magnetic moment by ∼0.06 μ_B atom^{-1} in terminations A and B of the ($\bar{1}11$) surface. However, the magnetic moment is lower at 0.298 μ_B atom^{-1} and larger at 0.382 μ_B atom^{-1} for the O ions in terminations A and B, respectively, compared to those in the bulk.

The work function (Φ), which measures the energy required to move an electron from the Fermi level (E_F) to the vacuum, was calculated as the difference between the potential of the vacuum (E_{vac}) and E_F. Based on this descriptor, the most reactive system is termination A of the Cu$_2$O(111) surface, since it only requires 4.831 eV of energy to provide the electron that can facilitate the detection of an adsorbed chemical species. However, termination A, which is the most stable plane of the CuO($\bar{1}11$) surface, has the largest work function of any of the pristine facets reported in this study at $\Phi = 5.943$ eV. Our results suggest that the different magnetic properties and stoichiometries of the Cu$_2$O(111) and CuO($\bar{1}11$) surfaces play major roles in the different trends observed for the work function values of terminations A and B for these materials. Moreover, the difference of the work function values is 0.192 eV for the least-stable terminations B of the Cu$_2$O(111) and CuO($\bar{1}11$) surfaces. Our simulated work function values suggest that TiO$_2$(111) has an intermediate reactivity between those of the terminations A of Cu$_2$O(111) and CuO($\bar{1}11$).

3.7. Simulation of the Multi-Nanolayer-Based Heterojunctions.

Based on the results for the pristine surfaces, we analyzed the thermodynamic stability, atomic structure, and electronic properties of the binary CuO($\bar{1}11$)/Cu$_2$O(111) and ternary TiO$_2$(111)/CuO($\bar{1}11$)/Cu$_2$O(111) multi-nanolayered interfaces with hexagonal symmetry. For the binary CuO($\bar{1}11$)/Cu$_2$O(111) heterojunction, we used the 1×1 surface geometry. For the ternary heterostructure TiO$_2$(111)/CuO($\bar{1}11$)/Cu$_2$O-(111), we employed the 1×2 supercell. Since we will investigate the adsorption properties of the 2×2 ternary heterojunction interfaces in section 3.8, we decided to simulate these structures using two, one, and four stoichiometric stacking sequences for Cu$_2$O(111), CuO($\bar{1}11$,) and TiO$_2$(111), respectively. This configuration ensures that we model 2×2 ternary heterojunctions that are approximately 10.63 Å in width and contain 104 atoms, as bigger systems have a prohibitively larger computational cost. We report these heterostructures using the most-stable termination A calculated for CuO($\bar{1}11$) and Cu$_2$O(111) and the only termination of TiO$_2$(111). All surfaces are comprised of incomplete top layers of O atoms, which are complementary in a "jigsaw puzzle" fashion and thus allow the subsurface Cu and Ti ions with dangling bonds to increase their coordination numbers. For the interface computations, we used the equilibrium lattice vectors for Cu$_2$O(111) to mimic the heteroepitaxial growth of CuO($\bar{1}11$) and then the TiO$_2$(111)

adlayers. Cu$_2$O(111) is perfectly hexagonal, but CuO($\bar{1}11$) and TiO$_2$(111) have monoclinic symmetries, leading to a mismatch of their lattice parameters and angles. Figure 10 displays the side
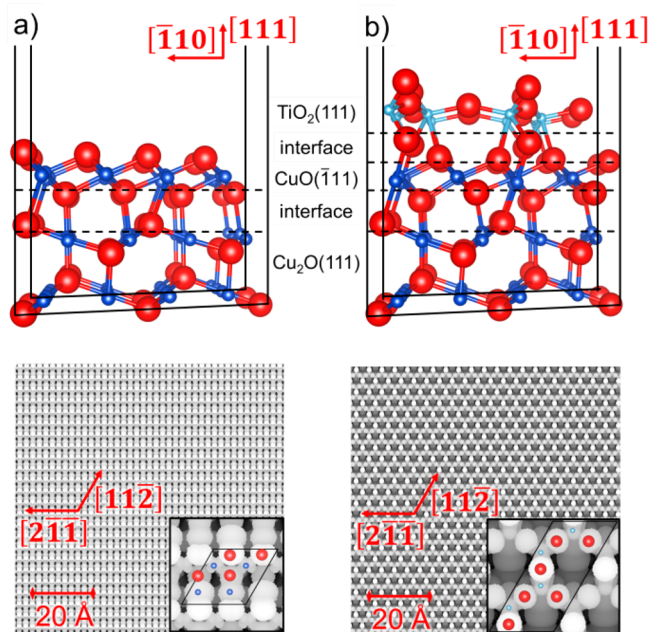

Figure 10. Top panels show the structure of the (a) binary CuO($\bar{1}11$)/Cu$_2$O(111) and (b) ternary TiO$_2$(111)/CuO($\bar{1}11$)/Cu$_2$O(111) interfaces. Bottom panels display the simulated scanning tunnelling microscopy (STM) images using a bias of (a) $V = 1.0$ eV or (b) $V = -0.5$ eV, a density of (a) $\rho = 0.0025$ e Å^{-3} or (b) $\rho = 0.0010$ e Å^{-3}, and a tip distance of: (a) $d = 1.21$ Å or (b) $d = 1.62$ Å. Crystallographic directions are indicated with respect to the Cu$_2$O(111) substrate. O atoms are shown in red, Cu atoms are shown in dark blue, and Ti atoms are shown in light blue.

views of the supercell slabs used to simulate the binary and ternary heteroepitaxial junctions. After the formation of CuO($\bar{1}11$)/Cu$_2$O(111), 50% of the exposed Cu atoms and 25% of the subsurface Cu atoms experience an outward relaxation of approximately 0.13 Å with respect to the pristine surfaces. Moreover, 50% of the subsurface anions shift their positions by ∼0.22 Å toward the surface in the binary device compared to those of the isolated materials. Our calculations suggest that the remaining atoms in the binary heterostructure suffer only a relatively smaller displacement after the deposition of the CuO($\bar{1}11$) layer. Next, we applied a layer of TiO$_2$(111) and found that all the Ti atoms relaxed toward the bulk to roughly form a single atomic layer in the ternary heterostructure, which is similar to the atomic displacements of the pristine surface.

The scanning tunnelling microscopy images (STM) were constructed using the basic formulation of the Tersoff−Hamann approach[71] as implemented in the HIVE code,[72] which was successfully employed in previous works to provide images in agreement with experiments.[66,73,74] The sign of the sample bias applied for the production of the STM images provides information on the valence of the conduction bands in the vicinity of the Fermi level (E_F). For example, the positive (negative) bias of $V = 1.0$ (-0.5) eV applied for the production of the STM image of the binary (ternary) heterostructure indicates that the electrons are moving from the probe tip to the conduction band (from the valence band to the probe tip). The
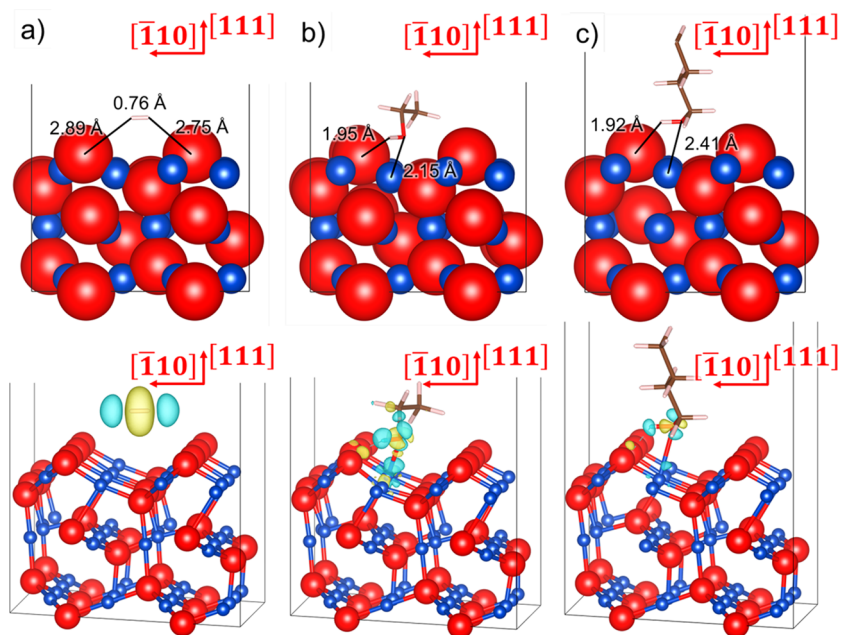
Figure 11. Adsorption of (a) H_2, (b) C_2H_5OH, and (c) n-C_4H_9OH on the $CuO(\bar{1}11)/Cu_2O(111)$ heterostructure. Interatomic distances are indicated in the top panels, while the charge density flow ($\Delta\rho$) is represented in the bottom panels. Electron density gain and depletion regions are shown in yellow and green, respectively. Isosurfaces display a value of ±0.005 e $Å^{-3}$. Crystallographic directions are indicated with respect to the $Cu_2O(111)$ substrate. The binary heterostructures are displayed using the (top panels) space-filling and (bottom panels) ball-and-stick representations, whereas the adsorbates are shown using the stick representation. O atoms are shown in red, H atoms are shown in white, C atoms are shown in brown, and Cu atoms are shown in dark blue.

brightest spots resolved for the surface of the binary $CuO(\bar{1}11)/Cu_2O(111)$ device correspond to the protruding O atoms located at the ridges along the $[2\bar{1}\bar{1}]$ direction, as shown in Figure 10a. The image also resolves the O atoms situated at the grooves, whose lowest brightness can be used to evaluate their relative position with respect to the anions at the tip of the ridge. Three- and fourfold Cu atoms can be seen, and their different sizes can also be used to differentiate them. Figure 10b clearly displays the honeycomb structure of the ternary $TiO_2(111)/CuO(\bar{1}11)/Cu_2O(111)$ interface whose corners are defined by O, which is represented by the brightest spots. Although Ti ions are the least noticeable ions, they are still well-defined circles that occupy the trigonal holes created by the O atoms.

Table S4 lists the geometric misfit parameter (ζ) that was quantified as $\zeta = 100 \cdot [1 - 2\Omega/(A_1 + A_2)]$, where Ω is the overlap area and A_1 and A_2 are the surface areas of the materials that form the interface.[75,76] The geometric misfit parameter is just under 1.7% for the binary heterojunction and 6.97% for the ternary interface. Note that the misfit parameter is typically below 5% for stable heteroepitaxial junctions, but much larger values such as 18.6% and 8.3% have been measured for $ZnO(0001)/Al_2O_3(0001)$ and $MgO(111)/Al_2O_3(0001)$, respectively.[77] The values of this parameter indicate that the thin-film $CuO(\bar{1}11)$ suffered a compression smaller than the expansion experienced by the TiO_2-based layer upon deposition onto the substrate.

The interfacial free energy (σ_{int}) was calculated as

$$\sigma_{int} = \gamma_r + (E_{int} - n_{over}E_{over} - E_{sub})/A \qquad (4)$$

where E_{int} and E_{sub} are the energies of the interface and substrate, respectively, E_{over} is the energy of 1 formula unit in the bulk of the overlayer, and n_{over} is the number of f.u. in the overlayer.

The interfacial free energy calculated for both heteroepitaxial systems is positive, implying that these interfaces are stable with respect to their isolated bulk components. The difference in interfacial energy for the binary and ternary heterostructures is only 21 meV $Å^{-2}$ despite the large difference in their geometric misfit parameters. Note that the interfacial free energy of the interfaces is larger and therefore less stable than the relaxed surface energy of the substrate $Cu_2O(111)$, explaining the carefully controlled experimental conditions required to prepare them. The calculated Bader charge is 0.139 e^- smaller for the exposed Cu atoms in $CuO(\bar{1}11)/Cu_2O(111)$ than that in pristine $CuO(\bar{1}11)$ surface. However, the subsequent deposition of the thin-film $TiO_2(111)$ increases the charge of the Ti atoms by only 0.024 e^- with respect to that of its pure surface. The formation of the binary heterojunction forces a large (modest) reduction of the magnetic moment by 0.448 (0.174) μ_B atom^{-1} of the Cu (O) ions compared to the value in the perfect $CuO(\bar{1}11)$ surface. Our simulations indicate that the magnetization of the middle $CuO(\bar{1}11)$ thin film induces magnetic moments one order of magnitude smaller on the atoms of the $TiO_2(111)$ top layer. The DFT modeling indicates that the deposition of the $CuO(\bar{1}11)$ layer onto the substrate raises the work function by 1.454 eV with respect to the value of this descriptor in the pristine $Cu_2O(111)$ surface. Likewise, the formation of the ternary heteroepitaxial junction leads to a further 1.169 eV increase of the work function of the nanodevice.

3.8. Simulation of the Molecular Adsorption Properties. We next investigated the adsorption properties of the binary and ternary layered heterojunction devices. We have considered the interaction of the single molecules probed experimentally, i.e., H_2, C_2H_5OH, and n-C_4H_9OH, with the symmetrically inequivalent adsorption sites. We believe that these early molecular adsorption processes will determine the kinetics of the oxidation reactions that are discussed within the oxygen chemisorption model in the Text S4 (Supporting Information). The O atoms from the VOC molecules were
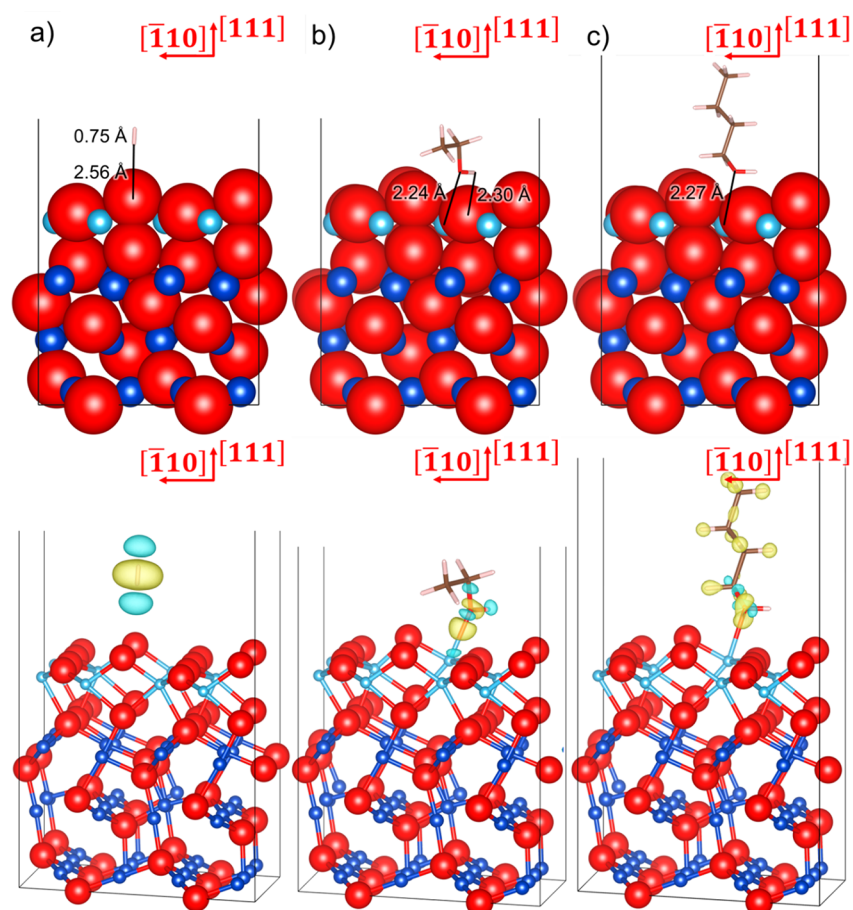
Figure 12. Adsorption of (a) H_2, (b) C_2H_5OH, and (c) n-C_4H_9OH on the $TiO_2(111)/CuO(\bar{1}11)/Cu_2O(111)$ heterostructure. Interatomic distances are indicated in the top panels, while the charge density flow ($\Delta\rho$) is represented in the bottom panels. Electron density gain and depletion regions are shown in yellow and green, respectively. Isosurfaces display a value of ±0.005 e Å^{-3}. Crystallographic directions are indicated with respect to the $Cu_2O(111)$ substrate. The ternary heterostructures are displayed using the (top panels) space-filling and (bottom panels) ball-and-stick representations, whereas the adsorbates are shown using the stick representation. O atoms are shown in red, H atoms are shown in white, C atoms are shown in brown, Cu atoms are shown in dark blue, and Ti atoms are shown in light blue.

initially placed 1.5 Å away from the closest transition metal atom of the sensing device and then subsequently optimized to their equilibrium configurations and energies. For the pristine heterostructures, the H_2 molecule was introduced to instead interact with the surface O atoms. Previous studies of nanosensor devices based on ZnO have shown that interactions between these atoms of opposite Coulomb charges lead to the most stable adsorption configurations.[78,79]

Table S5 lists the adsorption energies for the binding of the VOCs and molecular hydrogen onto both the exposed Cu and O atoms, respectively, of the binary heteroepitaxial structure $CuO(\bar{1}11)/Cu_2O(111)$. The largest adsorption energy $E_{ads} = -1.072$ eV was calculated for C_2H_5OH, which was followed by $E_{ads} = -0.833$ eV for n-C_4H_9OH on the most-reactive under-coordinated threefold Cu site of the binary layered device. From a thermodynamic point of view, C_2H_5OH and n-C_4H_9OH have binding strengths toward the under-coordinated threefold Cu site that are ~0.3 and ~0.05 eV larger, respectively, than their fully coordinated planar fourfold counterpart. Moreover, the difference is also 0.05 eV for the energy released by the H_2 molecule on the two types of O atoms. Our simulations suggest that H_2 shows the lowest preference for the binary heterostructure, which is in agreement with the low gas response reported for this gas from the experiments. We found that the incorporation of the $TiO_2(111)$ layer into the sensing device

reduces the number of symmetrically inequivalent adsorption sites to one type of O atom and one type of Ti atom. The binding energy of the alcohol with the lowest (largest) molecular weight is approximately 0.22 (0.08) eV lower on the Ti positions of the ternary heterostructure with respect to the Cu atom of $CuO(\bar{1}11)/Cu_2O(111)$. However, the energetic preference of H_2 becomes larger by just 0.01 eV on the O site of $TiO_2(111)/CuO(\bar{1}11)/Cu_2O(111)$ compared to the exposed anion on the binary heterojunction. The decreasing order of binding strength found for the alcohols on the Ti site and H_2 on the O position is $E_{ads}(H_2) \gg E_{ads}(n\text{-}C_4H_9OH) > E_{ads}(C_2H_5OH)$.

Figures 11 and 12 illustrate the most-favorable molecular adsorption modes of H_2 and the alcohols on the surface of the binary and ternary heterojunctions, which are in agreement with previous studies.[78,79] The small H_2 molecule is adsorbed almost perpendicularly to the surface on a threefold O site lying in the ridge along the $[2\bar{1}\bar{1}]$ direction. This is the weakest interaction reported in this study, which is characterized by an interfacial H−O distance of 2.43 Å. H_2 was also initially placed above a fourfold O atom in the groove along the $[2\bar{1}\bar{1}]$ direction but moved outward during optimization. In the resulting adsorption, H_2 forms a bidentate binuclear mode, since it lies flat to the surface, spanning the gap between two opposite threefold O atoms in parallel ridges, as displayed in Figure 11a. The results from the calculations indicate that the H−O distance between

H_2 and the surface is 0.14 Å larger across the threefold Cu side than across the fourfold Cu side. Nevertheless, the interaction with the surface led to a negligible stretching by 0.01 Å of the intra-atomic H−H distance with respect to that of the isolated molecule, but only for the adsorption at the groove site. We did not find evidence of H_2 dissociation in our calculations and thus speculate that this process is unlikely from a thermodynamic point of view. We found that the O of C_2H_5OH binds the surface three- and four-fold Cu atoms at 2.15 and 2.43 Å, respectively, as shown in Figure 11a. Given its small size, this molecule is able to place itself parallel to the surface grooves along the $[2\bar{1}\bar{1}]$ direction by forming hydrogen bonds to the exposed threefold O atoms at the top of the ridge. Interestingly, we calculated the shortest distance of 1.95 Å for the interaction between the hydroxyl H and the surface O of the $[CuO_{3/2}]$ unit nearest to the coordinated threefold Cu. However, C_2H_5OH forms hydrogen bonds with the O that belongs to the same $[CuO_{4/2}]$ unit of the coordinated fourfold Cu atom at the largest distance of 2.02 Å. The shortest distances for the interaction of C_2H_5OH at the threefold Cu position explain our strongest calculated DFT adsorption energy for this site. We observed a difference of just 0.08 Å for the interfacial bond distances between the three- and fourfold Cu sites and the O atoms for the heavier n-C_4H_9OH molecule (see Figure 11c). Moreover, the hydrogen bond distance between the OH group and the surface threefold O atoms is 1.92 Å for both adsorption configurations investigated here. Unlike C_2H_5OH, the large and nonpolar hydrocarbon chain of n-C_4H_9OH prefers to adsorb perpendicular to the surface plane for the interaction with the three- and fourfold Cu sites. Thus, this provides n-C_4H_9OH with the appropriate orientation and separation from the heterostructure to form its hydrogen bond to the surface O atom directly bound to the coordinated Cu atom. We rationalized the trend of the adsorption energies of the VOCs based on their interatomic distances to the surface, which are inversely proportional.

We have integrated the Bader charges, which indicate that the largest transfer of $\Delta q = -0.119$ e$^-$ was found for the adsorption of the electron-rich H_2 molecule at the tetrahedral sp^3 dangling bond position of the ridge threefold O atom, as summarized in Table S5. Based on the large electronegative difference of $\Delta\chi_{HO} = 1.24$ (Pauling scale),[80] this adsorption geometry promoted an effective charge transfer mechanism from the adsorbate to the surface. Surprisingly, the smallest charge transfer takes place from the surface to the bidentate binuclear H_2 in the adsorption at the groove position, since the adsorbate is not in a configuration that facilitates appropriate orbital overlap with the exposed O atoms. Figure 11a illustrates that the interfacial charge transfer vanishes for this adsorption mode, with the electron-rich region located between the H atoms similar to the filled σ_{1s}^{b2} bonding molecular orbital and the electron-depleted regions σ_{1s}^*, which represent the empty antibonding molecular orbital, all lying on the symmetry axis. Moreover, all VOC molecules lost electronic density upon their adsorption onto the binary heteroepitaxial junction, with the observed charge flow values in line with the trend of simulated adsorption energies. Figure 11a and b displays the charge rearrangements between the OH group of the VOCs and the surface Cu and O atoms of the binary heterostructure, which are more noticeable for C_2H_5OH than for n-C_4H_9OH.

The incorporation of TiO_2 does not noticeably change the most stable adsorption geometries for the VOCs with respect to the binary sensor but instead affects the interaction configuration for H_2 (see Figure 12a). For the most-stable adsorption,

we found that H_2 prefers to sit perpendicularly to the $TiO_2(111)$ layer 2.56 Å above any of the quasi-equivalent O atoms. H_2 is only able to coordinate a single anion since this surface does not form grooves with under-coordinated O atoms at the top of the ridges, which allow the flat bidentate binuclear adsorption of the molecule. Figure 12b illustrates that C_2H_5OH also coordinates an exposed Ti ion via its hydroxyl O atom, but the molecule adsorbs 0.09 Å further from the surface site than it does in the case of $CuO(\bar{1}11)/Cu_2O(111)$. Given the close proximity of the surface Ti and O atoms, C_2H_5OH cannot form a strong interfacial hydrogen bond, with the H···O distance stretched to the atypical value of 2.30 Å. n-C_4H_9OH also forms an adsorption mode on the surface of $TiO_2(111)/CuO(\bar{1}11)/Cu_2O(111)$ that is more detached than that in the binary device, which even prevents the formation of a hydrogen bond with the exposed O atoms as shown in Figure 12c. We found that the computed charge transfers between the adsorbates and the ternary device explain their adsorption energy values (see Table S5). For example, the charge transfer is almost zero for H_2, suggesting physisorption and agreeing with its lowest adsorption energies, whereas the VOC molecules donate electron density to the surface, agreeing with the strength of their adsorptions. The charge transfers for the VOCs are also smaller for the ternary device than for the binary heterostructure, which compares well with and explains their relative adsorption energy values. Figure 12a shows the intramolecular charge redistribution that resembles the molecular orbitals of H_2, with a negligible influence of the surface of the sensor. The Ti ion that coordinates the OH group of C_2H_5OH loses some electronic density charge, whereas the cation that coordinates the O atom of n-C_4H_9OH is the least perturbed for any VOC molecule (see Figure 12b and c).

We have provided strong evidence that the change in the sensitivity is the consequence of applying a layer of $TiO_2(111)$ to the $CuO(\bar{1}11)/Cu_2O(111)$ sensing device. Our DFT calculations show that the ternary heteroepitaxial junction displays smaller adsorption energies toward the VOCs than toward the binary nanodevice, which agrees with the gas response experiments discussed in section 3.4. We have rationalized the different behaviors of the $CuO(\bar{1}11)/Cu_2O$-(111) and $TiO_2(111)/CuO(\bar{1}11)/Cu_2O(111)$ heterojunctions based on their atomic charges and surface structures. The Bader charges calculated for both $q_{Ti} = +2.235$ e$^-$ and $q_O = -1.130$ e$^-$ in the ternary device are larger than those calculated for $q_{Cu} = +0.867$ e$^-$ and $q_O = -0.965$e$^-$ in the binary heterostructure. This supports a Coulombic attraction between an equally spaced OH group of the VOCs and the surface of $TiO_2(111)/CuO(\bar{1}11)/Cu_2O(111)$ that is stronger than the facet of the binary material. On the other hand, the separation of 3.29 Å between the exposed Cu and O atoms in neighboring $[CuO_{3/2}]$ units allows the efficient formation of both coordinate and hydrogen bonds between the $CuO(\bar{1}11)/Cu_2O(111)$ heteroepitaxial material and the OH group of the VOCs. However, the relative position and 1.90 Å separation between the surface counterions prevent the simultaneous formation of the Ti−OH and OH···O bonds between the adsorbate molecule and the $TiO_2(111)/CuO$-$(\bar{1}11)/Cu_2O(111)$ heterojunction. Our DFT simulations suggest that the alcohols show a larger preference toward the formation of the Ti−OH coordinate bond instead of a hydrogen bond with the ternary heterostructure given the larger Coulombic attraction of the former type of interaction compared to the latter one. Moreover, the modeling indicates that the surface structure and relative position of the atoms plays

a more important role than the Bader charges in determining the geometries and adsorption energies of the VOCs. Nonpolar H_2 is the only molecule that shows both a physisorbed mode on the $CuO(\bar{1}11)/Cu_2O(111)$ sensor with a larger adsorption energy than the chemisorbed configuration. Although it is the least favorable of all adsorbates explored here, H_2 is also the only molecule that displays a slightly larger adsorption energy for its physisorption mode on the ternary device than on the binary device. Thus, the calculations that we have carried out offer an additional and complementary understanding, from a molecular point of view, into the sensing mechanism of the binary and ternary heteroepitaxial junctions.

4. CONCLUSIONS

In this paper we have studied the heterostructure of mixed titania/cuprite/cupric oxide ($TiO_2/CuO/Cu_2O$) phases that were obtained via a facile, cost-effective, simple, and reliable spray—sputtering—annealing approach. The investigated mixed oxide semiconductor phases are nanocrystalline and possess direct optical band gaps that are preferred for sensing applications, owing to the direct recombination with the release of energy. We have discussed the properties and enhanced gas detecting characteristics of the CuO/Cu_2O nanolayered heterojunction device structure that is based on two precise phases, i.e., CuO and Cu_2O. The effect of different thicknesses on the sensor performances is reported for the CuO/Cu_2O nanolayered crystalline heterojunction as well. The method presented in this work allows for the preparation of high-quality nanomaterials with different compositions and crystal phases. CuO/Cu_2O nanolayers with thicknesses between 20 and 30 nm, which were prepared using conventional thermal annealing at 420 °C for 0.5 h, stand out for having promising sensing characteristics in terms of a good selectivity and a high response to volatile organic compounds. The best results, with a response of about 150% to 100 ppm of ethanol, were achieved at a working temperature of 350 °C.

The CuO/Cu_2O samples show a high selectivity and response to ethanol, which improved alongside the long-term stability of the sensor after covering the surface with a thin layer of titania TiO_2. We also noted that even after the deposition of titanium oxide, the response to ethanol did not change significantly. In general, p-type semiconducting oxides, such as CuO/Cu_2O, will allow a complete reaction of ethanol, which will result in increasing sensing performances toward its vapors. We also found that the response to ethanol vapors decreased for the CuO/Cu_2O samples, whereas it remained unchanged in the case of the $TiO_2/CuO/Cu_2O$ samples with respect to the temperature. Significant changes were not observed due to the self-cleaning effect of the ternary heterostructure.[55,56] These results provide evidence that the deposited thin TiO_2 film protects the sensor, increasing its lifespan. Thus, the titania (TiO_2) ultrathin layers deposited on top of CuO/Cu_2O using the spray pyrolysis method can be used for the long-term stabilization of the functionalities of the sensors and to provide protection against corrosion at high temperatures.[27−30,55,56]

We have used first-principles techniques to simulate the formation of the binary $CuO(\bar{1}11)/Cu_2O(111)$ and ternary $TiO_2(111)/CuO(\bar{1}11)/Cu_2O(111)$ heterostructures in addition to their reactivities toward H_2, C_2H_5OH, and $n\text{-}C_4H_9OH$. We have investigated the deposition of the monoclinic $CuO(\bar{1}11)$ and $TiO_2(111)$ thin-film overlayers on the Cu_2O-(111) surface substrate with a hexagonal symmetry and found that these are thermodynamically stable systems despite the

lattice mismatch. The binary and ternary heterostructures are thermodynamically stable. The value of the work function rises with the number of components of the heterojunctions, which is consistent with their different sensitivities. The study of the affinity of the VOCs and H_2 toward the binary and ternary heterostructures shows that the adsorbates interact molecularly with the surface of the sensors. H_2 and C_2H_5OH release the smallest and largest adsorption energies in their ground-state interaction configurations, respectively, on the surfaces of both nanodevices, which is in agreement with their similar selectivities. The electronic properties of the ground-state adsorption configurations alongside the surface structure are important descriptors that explain the trends of the binding energies.

ASSOCIATED CONTENT

ⓈⒾ Supporting Information

The Supporting Information is available free of charge at https://pubs.acs.org/doi/10.1021/acsami.1c04379.

computation details of the DFT calculations, cross-section views of device set #1 and device set #2, micro-Raman spectra, cubic unit cell of the Cu_2O lattice, zone centre normal modes, transmission sectra, plots of the $(\alpha h\nu)^2$ vs photon energy for the CuO/Cu_2O and $TiO_2/CuO/Cu_2O$ heterostructures, dynamic and gas response curves, sensing mechanism, energy band diagrams, calculated and experimental parameters, side and top views of the optimized structures, crystallographic directions and sequence stacking, surface energies, and SEM images (PDF)

AUTHOR INFORMATION

Corresponding Authors

Oleg Lupan — *Functional Nanomaterials, Faculty of Engineering, Institute for Materials Science, Kiel University, D-24143 Kiel, Germany; Center for Nanotechnology and Nanosensors, Technical University of Moldova, MD-2004 Chisinau, Republic of Moldova; Department of Physics, University of Central Florida, Orlando, Florida 32816-2385, United States;* ⓞ orcid.org/0000-0002-7913-9712; Email: ollu@tf.uni-kiel.de, oleg.lupan@mib.utm.md

Rainer Adelung — *Functional Nanomaterials, Faculty of Engineering, Institute for Materials Science, Kiel University, D-24143 Kiel, Germany;* Email: ra@tf.uni-kiel.de

Sandra Hansen — *Functional Nanomaterials, Faculty of Engineering, Institute for Materials Science, Kiel University, D-24143 Kiel, Germany;* ⓞ orcid.org/0000-0002-3529-8367; Email: sn@tf.uni-kiel.de

Franz Faupel — *Faculty of Engineering, Chair for Multicomponent Materials, Christian-Albrechts Universität zu Kiel, D-24143 16 Kiel, Germany;* ⓞ orcid.org/0000-0003-3367-1655; Email: ff@tf.uni-kiel.de

David Santos-Carballal — *School of Chemistry, University of Leeds, Leeds LS2 9JT, United Kingdom;* ⓞ orcid.org/0000-0002-3199-9588; Email: d.santos-carballal@leeds.ac.uk

Authors

Nicolai Ababii — *Center for Nanotechnology and Nanosensors, Technical University of Moldova, MD-2004 Chisinau, Republic of Moldova*

Nicolae Magariu — *Center for Nanotechnology and Nanosensors, Technical University of Moldova, MD-2004 Chisinau, Republic of Moldova*

Alexander Vahl — *Faculty of Engineering, Chair for Multicomponent Materials, Christian-Albrechts Universität zu Kiel, D-24143 16 Kiel, Germany*

Lukas Zimoch — *Functional Nanomaterials, Faculty of Engineering, Institute for Materials Science, Kiel University, D-24143 Kiel, Germany*

Mathias Hoppe — *Functional Nanomaterials, Faculty of Engineering, Institute for Materials Science, Kiel University, D-24143 Kiel, Germany*

Thierry Pauporté — *Institut de Recherche de Chimie Paris-IRCP, Chimie ParisTech, Paris Sciences et Lettres (PSL) Université, 75231 Paris, France*

Vardan Galstyan — *Sensor Laboratory, Department of Information Engineering (DII), University of Brescia, 25133 Brescia, Italy;* orcid.org/0000-0002-0615-3097

Victor Sontea — *National Center for Biomedical Engineering, Technical University of Moldova, MD-2004 Chisinau, Republic of Moldova; Department of Nanoelectronics and Surface Modification, Sumy State University, 40007 Sumy, Ukraine*

Lee Chow — *Department of Physics, University of Central Florida, Orlando, Florida 32816-2385, United States*

Nora H de Leeuw — *School of Chemistry, University of Leeds, Leeds LS2 9JT, United Kingdom; Department of Earth Sciences, Utrecht University, 3584 CD Utrecht, The Netherlands*

Elisabetta Comini — *Sensor Laboratory, Department of Information Engineering (DII), University of Brescia, 25133 Brescia, Italy;* orcid.org/0000-0003-2559-5197

Complete contact information is available at:
https://pubs.acs.org/10.1021/acsami.1c04379

Author Contributions

O.L., N.A., M.H., and L.Z. synthesized the CuO/Cu2O/Cu nanomaterials and developed the synthesis methodology. A.V. and F.F. performed all XPS investigations, analyzed the XPS results, and drafted part of the article. O.L., N.A., E.C., V.G., and S.N. fitted a technological procedure for micronanomaterial integration into the devices for detecting VOCs. N.A., V.G., E.C., and O.L. realized the measurement of the detecting characteristics of the CuO/Cu2O/Cu materials, analyzed the data, and drafted part of the article. Th.P. and O.L. performed the optical measurements. Th.P. performed the titania deposition. O.L., D.S.-C., N.A., A.V., E.C., N.H.d.L., R.A., V.G., and S.H. analyzed the data from experiments and worked on the manuscript. D.S.-C., and N.H.d.L. carried out the DFT simulations and drafted the computational part of the article. O.L., R.A., E.C., F.F., N.A., L.C., S.N., N.H.d.L., and D.S.-C. conceived and designed the study and gave the final approval of the draft to be submitted and published. O.L., E.C., L.C., and R.A. performed the design and conception for the studies and gave the final approval. The work was written based on contributions by all authors, all of whom reviewed the manuscript.

Notes

The authors declare no competing financial interest.

REFERENCES

(1) Hoppe, M.; Ababii, N.; Postica, V.; Lupan, O.; Polonskyi, O.; Schütt, F.; Kaps, S.; Sukhodub, L. F.; Sontea, V.; Strunskus, T.; Faupel, F.; Adelung, R. (CuO-Cu2O)/ZnO:Al Heterojunctions for Volatile Organic Compound Detection. *Sens. Actuators, B* **2018**, *255*, 1362−1375.

(2) Zappa, D.; Galstyan, V.; Kaur, N.; Munasinghe Arachchige, H. M. M.; Sisman, O.; Comini, E. Metal Oxide -Based Heterostructures for Gas Sensors"- A Review. *Anal. Chim. Acta* **2018**, *1039*, 1−23.

(3) Su, C.; Zhang, L.; Han, Y.; Ren, C.; Li, B.; Wang, T.; Zeng, M.; Su, Y.; Hu, N.; Zhou, Z.; Wang, Y.; Yang, Z.; Xu, L. Glucose-Assisted Synthesis of Hierarchical NiO-ZnO Heterostructure with Enhanced Glycol Gas Sensing Performance. *Sens. Actuators, B* **2021**, *329*, 129167.

(4) Nordseth, Ø.; Kumar, R.; Bergum, K.; Fara, L.; Dumitru, C.; Craciunescu, D.; Dragan, F.; Chilibon, I.; Monakhov, E.; Foss, S.; Svensson, B. Metal Oxide Thin-Film Heterojunctions for Photovoltaic Applications. *Materials* **2018**, *11* (12), 2593.

(5) Wu, E.; Xie, Y.; Yuan, B.; Zhang, H.; Hu, X.; Liu, J.; Zhang, D. Ultrasensitive and Fully Reversible NO2 Gas Sensing Based on P-Type MoTe2 under Ultraviolet Illumination. *ACS Sensors* **2018**, *3* (9), 1719−1726.

(6) Lupan, O.; Cretu, V.; Postica, V.; Polonskyi, O.; Ababii, N.; Schütt, F.; Kaidas, V.; Faupel, F.; Adelung, R. Non-Planar Nanoscale p−p Heterojunctions Formation in Zn$_x$Cu$_{1-x}$O$_y$ Nanocrystals by Mixed Phases for Enhanced Sensors. *Sens. Actuators, B* **2016**, *230*, 832−843.

(7) Brattain, W. H.; Bardeen, J. Surface Properties of Germanium. *Bell Syst. Tech. J.* **1953**, *32* (1), 1−41.

(8) McWilliams, S.; Flynn, C. D.; McWilliams, J.; Arnold, D. C.; Wahyuono, R. A.; Undisz, A.; Rettenmayr, M.; Ignaszak, A. Nano-structured Cu2O Synthesized via Bipolar Electrochemistry. *Nanomaterials* **2019**, *9* (12), 1781.

(9) Verma, N.; Kumar, N. Synthesis and Biomedical Applications of Copper Oxide Nanoparticles: An Expanding Horizon. *ACS Biomater. Sci. Eng.* **2019**, *5* (3), 1170−1188.

(10) Brattain, W. H. The Copper Oxide Rectifier. *Rev. Mod. Phys.* **1951**, *23* (3), 203−212.

(11) Lupan, O.; Postica, V.; Cretu, V.; Wolff, N.; Duppel, V.; Kienle, L.; Adelung, R. Single and Networked CuO Nanowires for Highly Sensitive P-Type Semiconductor Gas Sensor Applications. *Phys. Status Solidi RRL* **2016**, *10* (3), 260−266.

(12) Tiginyanu, I. M.; Lupan, O.; Ursaki, V. V.; Chow, L.; Enachi, M. Nanostructures of Metal Oxides. In *Comprehensive Semiconductor Science and Technology*, Vol. 3; Bhattacharya, P., Fornari, R., Kamimura, H., Eds.; Elsevier: Amsterdam, The Netherlands, 2011; pp 396−479.

(13) Bendavid, L. I.; Carter, E. A. First-Principles Predictions of the Structure, Stability, and Photocatalytic Potential of Cu2O Surfaces. *J. Phys. Chem. B* **2013**, *117* (49), 15750−15760.

(14) Siebert, L.; Lupan, O.; Mirabelli, M.; Ababii, N.; Terasa, M.-I.; Kaps, S.; Cretu, V.; Vahl, A.; Faupel, F.; Adelung, R. 3D-Printed

Chemiresistive Sensor Array on Nanowire CuO/Cu$_2$O/Cu Heterojunction Nets. *ACS Appl. Mater. Interfaces* **2019**, *11* (28), 25508−25515.

(15) Vahl, A.; Carstensen, J.; Kaps, S.; Lupan, O.; Strunskus, T.; Adelung, R.; Faupel, F. Concept and Modelling of Memsensors as Two Terminal Devices with Enhanced Capabilities in Neuromorphic Engineering. *Sci. Rep.* **2019**, *9* (1), 4361.

(16) Steinhauer, S. Gas Sensors Based on Copper Oxide Nanomaterials: A Review. *Chemosensors* **2021**, *9* (3), 51.

(17) Moseley, P. T. Progress in the Development of Semiconducting Metal Oxide Gas Sensors: A Review. *Meas. Sci. Technol.* **2017**, *28* (8), 082001.

(18) Kim, H.-J.; Lee, J.-H. Highly Sensitive and Selective Gas Sensors Using P-Type Oxide Semiconductors: Overview. *Sens. Actuators, B* **2014**, *192*, 607−627.

(19) Degler, D.; Weimar, U.; Barsan, N. Current Understanding of the Fundamental Mechanisms of Doped and Loaded Semiconducting Metal-Oxide-Based Gas Sensing Materials. *ACS Sensors* **2019**, *4* (9), 2228−2249.

(20) Saruhan, B.; Lontio Fomekong, R.; Nahirniak, S. Review: Influences of Semiconductor Metal Oxide Properties on Gas Sensing Characteristics. *Front. Sensors* **2021**, *2*, 2.

(21) Mishra, A. K.; Roldan, A.; de Leeuw, N. H. A Density Functional Theory Study of the Adsorption Behaviour of CO$_2$ on Cu$_2$O Surfaces. *J. Chem. Phys.* **2016**, *145* (4), 044709.

(22) Siegfried, M. J.; Choi, K.-S. Elucidating the Effect of Additives on the Growth and Stability of Cu$_2$O Surfaces via Shape Transformation of Pre-Grown Crystals. *J. Am. Chem. Soc.* **2006**, *128* (32), 10356−10357.

(23) Mishra, A. K.; Roldan, A.; de Leeuw, N. H. CuO Surfaces and CO$_2$ Activation: A Dispersion-Corrected DFT+ U Study. *J. Phys. Chem. C* **2016**, *120* (4), 2198−2214.

(24) Du, Y. E.; Feng, Q.; Chen, C.; Tanaka, Y.; Yang, X. Photocatalytic and Dye-Sensitized Solar Cell Performances of {010}- Faceted and [111]-Faceted Anatase TiO$_2$ Nanocrystals Synthesized from Tetratitanate Nanoribbons. *ACS Appl. Mater. Interfaces* **2014**, *6* (18), 16007−16019.

(25) Xu, H.; Reunchan, P.; Ouyang, S.; Tong, H.; Umezawa, N.; Kako, T.; Ye, J. Anatase TiO$_2$ Single Crystals Exposed with High-Reactive {111} Facets toward Efficient H$_2$ Evolution. *Chem. Mater.* **2013**, *25* (3), 405−411.

(26) Popov, A. P.; Priezzhev, A. V.; Lademann, J.; Myllylä, R. TiO$_2$ Nanoparticles as an Effective UV-B Radiation Skin-Protective Compound in Sunscreens. *J. Phys. D: Appl. Phys.* **2005**, *38* (15), 2564−2570.

(27) Veziroglu, S.; Hwang, J.; Drewes, J.; Barg, I.; Shondo, J.; Strunskus, T.; Polonskyi, O.; Faupel, F.; Aktas, O. C. PdO Nanoparticles Decorated TiO$_2$ Film with Enhanced Photocatalytic and Self-Cleaning Properties. *Mater. Today Chem.* **2020**, *16*, 100251.

(28) Abdeen, D.; El Hachach, M.; Koc, M.; Atieh, M. A Review on the Corrosion Behaviour of Nanocoatings on Metallic Substrates. *Materials* **2019**, *12* (2), 210.

(29) Boukerche, S.; Himour, A.; Bououdina, M.; Bensouici, F.; Ouchenane, S. Multilayered ZnO/TiO$_2$ Nanostructures as Efficient Corrosion Protection for Stainless Steel 304. *Mater. Res. Express* **2019**, *6* (5), 055052.

(30) Won, Y.; Schwartzenberg, K.; Gray, K. A. TiO$_2$-Based Transparent Coatings Create Self-Cleaning Surfaces. *Chemosphere* **2018**, *208*, 899−906.

(31) Zeng, G.; Wu, C.; Chang, Y.; Zhou, C.; Chen, B.; Zhang, M.; Li, J.; Duan, X.; Yang, Q.; Pang, W. Detection and Discrimination of Volatile Organic Compounds Using a Single Film Bulk Acoustic Wave Resonator with Temperature Modulation as a Multiparameter Virtual Sensor Array. *ACS Sensors* **2019**, *4* (6), 1524−1533.

(32) Righettoni, M.; Tricoli, A. Toward Portable Breath Acetone Analysis for Diabetes Detection. *J. Breath Res.* **2011**, *5* (3), 037109.

(33) Siebert, L.; Wolff, N.; Ababii, N.; Terasa, M.-I.; Lupan, O.; Vahl, A.; Duppel, V.; Qiu, H.; Tienken, M.; Mirabelli, M.; Sontea, V.; Faupel, F.; Kienle, L.; Adelung, R. Facile Fabrication of Semiconducting Oxide Nanostructures by Direct Ink Writing of Readily Available Metal Microparticles and Their Application as Low Power Acetone Gas Sensors. *Nano Energy* **2020**, *70*, 104420.

(34) Tassopoulos, C. N.; Barnett, D.; Russell Fraser, T. Breath-Acetone and Blood-Sugar Measurements in Diabetes. *Lancet* **1969**, *293* (7609), 1282−1286.

(35) Galstyan, V.; Poli, N.; D'Arco, A.; Macis, S.; Lupi, S.; Comini, E. A Novel Approach for Green Synthesis of WO$_3$ Nanomaterials and Their Highly Selective Chemical Sensing Properties. *J. Mater. Chem. A* **2020**, *8* (39), 20373−20385.

(36) Hakim, M.; Broza, Y. Y.; Barash, O.; Peled, N.; Phillips, M.; Amann, A.; Haick, H. Volatile Organic Compounds of Lung Cancer and Possible Biochemical Pathways. *Chem. Rev.* **2012**, *112* (11), 5949−5966.

(37) Adiguzel, Y.; Kulah, H. Breath Sensors for Lung Cancer Diagnosis. *Biosens. Bioelectron.* **2015**, *65*, 121−138.

(38) Suematsu, K.; Harano, W.; Oyama, T.; Shin, Y.; Watanabe, K.; Shimanoe, K. Pulse-Driven Semiconductor Gas Sensors Toward Ppt Level Toluene Detection. *Anal. Chem.* **2018**, *90* (19), 11219−11223.

(39) Krilaviciute, A.; Heiss, J. A.; Leja, M.; Kupcinskas, J.; Haick, H.; Brenner, H. Detection of Cancer through Exhaled Breath: A Systematic Review. *Oncotarget* **2015**, *6* (36), 38643−38657.

(40) Amann, A.; Mochalski, P.; Ruzsanyi, V.; Broza, Y. Y.; Haick, H. Assessment of the Exhalation Kinetics of Volatile Cancer Biomarkers Based on Their Physicochemical Properties. *J. Breath Res.* **2014**, *8* (1), 016003.

(41) Haick, H.; Broza, Y. Y.; Mochalski, P.; Ruzsanyi, V.; Amann, A. Assessment, Origin, and Implementation of Breath Volatile Cancer Markers. *Chem. Soc. Rev.* **2014**, *43* (5), 1423−1449.

(42) Ababii, N.; Hoppe, M.; Shree, S.; Vahl, A.; Ulfa, M.; Pauporté, T.; Viana, B.; Cretu, V.; Magariu, N.; Postica, V.; Sontea, V.; Terasa, M.-I.; Polonskyi, O.; Faupel, F.; Adelung, R.; Lupan, O. Effect of Noble Metal Functionalization and Film Thickness on Sensing Properties of Sprayed TiO$_2$ Ultra-Thin Films. *Sens. Actuators, A* **2019**, *293*, 242−258.

(43) Lupan, O.; Cretu, V.; Postica, V.; Ababii, N.; Polonskyi, O.; Kaidas, V.; Schütt, F.; Mishra, Y. K.; Monaico, E.; Tiginyanu, I.; Sontea, V.; Strunskus, T.; Faupel, F.; Adelung, R. Enhanced Ethanol Vapour Sensing Performances of Copper Oxide Nanocrystals with Mixed Phases. *Sens. Actuators, B* **2016**, *224*, 434−448.

(44) Wang, P.; Shao, Z.; Ulfa, M.; Pauporté, T. Insights into the Hole Blocking Layer Effect on the Perovskite Solar Cell Performance and Impedance Response. *J. Phys. Chem. C* **2017**, *121* (17), 9131−9141.

(45) Chow, L.; Lupan, O.; Heinrich, H.; Chai, G. Self-Assembly of Densely Packed and Aligned Bilayer ZnO Nanorod Arrays. *Appl. Phys. Lett.* **2009**, *94* (16), 163105.

(46) Lupan, O.; Postica, V.; Ababii, N.; Reimer, T.; Shree, S.; Hoppe, M.; Polonskyi, O.; Sontea, V.; Chemnitz, S.; Faupel, F.; Adelung, R. Ultra-Thin TiO$_2$ Films by Atomic Layer Deposition and Surface Functionalization with Au Nanodots for Sensing Applications. *Mater. Sci. Semicond. Process.* **2018**, *87*, 44−53.

(47) Pauporté, T.; Lupan, O.; Zhang, J.; Tugsuz, T.; Ciofini, I.; Labat, F.; Viana, B. Low-Temperature Preparation of Ag-Doped ZnO Nanowire Arrays, DFT Study, and Application to Light-Emitting Diode. *ACS Appl. Mater. Interfaces* **2015**, *7* (22), 11871−11880.

(48) Vahl, A.; Dittmann, J.; Jetter, J.; Veziroglu, S.; Shree, S.; Ababii, N.; Lupan, O.; Aktas, O. C.; Strunskus, T.; Quandt, E.; Adelung, R.; Sharma, S. K.; Faupel, F. The Impact of O$_2$/Ar Ratio on Morphology and Functional Properties in Reactive Sputtering of Metal Oxide Thin Films. *Nanotechnology* **2019**, *30* (23), 235603.

(49) Cretu, V.; Postica, V.; Mishra, A. K.; Hoppe, M.; Tiginyanu, I.; Mishra, Y. K.; Chow, L.; de Leeuw, N. H.; Adelung, R.; Lupan, O. Synthesis, Characterization and DFT Studies of Zinc-Doped Copper Oxide Nanocrystals for Gas Sensing Applications. *J. Mater. Chem. A* **2016**, *4* (17), 6527−6539.

(50) Pauly, N.; Tougaard, S.; Yubero, F. Determination of the Cu 2p Primary Excitation Spectra for Cu, Cu$_2$O and CuO. *Surf. Sci.* **2014**, *620*, 17−22.

(51) Moulder, J. F.; Stickle, W. F.; Sobol, P. E.; Bomben, K. D. *Handbook of X-Ray Photoelectron Spectroscopy: A Reference Book of Standard Spectra for Identification and Interpretation of XPS Data*;

Chastain, J., Ed.; Physical Electronics Division, Perkin-Elmer Corporation: Waltham, MA, 1992.

(52) Naumkin, A. V.; Kraut-Vass, A., Gaarenstroom, S. W.; Powell, C. J. NIST X-ray Photoelectron Spectroscopy Database. *NIST Standard Rereference Database 20*, ver. 4.1. National Institute of Standards and Technology, 2000 (accessed 2018−02−08).

(53) Wilson, R.; Simion, C.; Blackman, C.; Carmalt, C.; Stanoiu, A.; Di Maggio, F.; Covington, J. The Effect of Film Thickness on the Gas Sensing Properties of Ultra-Thin TiO_2 Films Deposited by Atomic Layer Deposition. *Sensors* 2018, *18* (3), 735.

(54) Hsu, C.-L.; Tsai, J.-Y.; Hsueh, T.-J. Ethanol Gas and Humidity Sensors of CuO/Cu_2O Composite Nanowires Based on a Cu through-Silicon via Approach. *Sens. Actuators, B* 2016, *224*, 95−102.

(55) Adachi, T.; Latthe, S. S.; Gosavi, S. W.; Roy, N.; Suzuki, N.; Ikari, H.; Kato, K.; Katsumata, K.; Nakata, K.; Furudate, M.; Inoue, T.; Kondo, T.; Yuasa, M.; Fujishima, A.; Terashima, C. Photocatalytic, Superhydrophilic, Self-Cleaning TiO_2 Coating on Cheap, Light-Weight, Flexible Polycarbonate Substrates. *Appl. Surf. Sci.* 2018, *458*, 917−923.

(56) Banerjee, S.; Dionysiou, D. D.; Pillai, S. C. Self-Cleaning Applications of TiO_2 by Photo-Induced Hydrophilicity and Photo-catalysis. *Appl. Catal., B* 2015, *176−177*, 396−428.

(57) Barsan, N.; Schweizer-Berberich, M.; Göpel, W. Fundamental and Practical Aspects in the Design of Nanoscaled SnO_2 Gas Sensors: A Status Report. *Fresenius' J. Anal. Chem.* 1999, *365* (4), 287−304.

(58) Foo, M. L.; Huang, Q.; Lynn, J. W.; Lee, W. L.; Klimczuk, T.; Hagemann, I. S.; Ong, N. P.; Cava, R. J. Synthesis, Structure and Physical Properties of Ru Ferrites: $BaMRu_5O_{11}$ (*M*=Li and Cu) and $BaM'_2Ru_4O_{11}$ (*M'*=Mn, Fe and Co). *J. Solid State Chem.* 2006, *179* (2), 563−572.

(59) Downie, L. J.; Black, C.; Ardashnikova, E. I.; Tang, C. C.; Vasiliev, A. N.; Golovanov, A. N.; Berdonosov, P. S.; Dolgikh, V. A.; Lightfoot, P. Structural Phase Transitions in the Kagome Lattice Based Materials $Cs_{2-x}Rb_xSnCu_3F_{12}$ (x = 0, 0.5, 1.0, 1.5). *CrystEngComm* 2014, *16* (32), 7419−7425.

(60) Kliche, G.; Popovic, Z. V. Far-Infrared Spectroscopic Investigations on CuO. *Phys. Rev. B: Condens. Matter Mater. Phys.* 1990, *42* (16), 10060−10066.

(61) Leinekugel-le-Cocq-Errien, A. Y.; Deniard, P.; Jobic, S.; Gautier, E.; Evain, M.; Aubin, V.; Bart, F. Structural Characterization of the Hollandite Host Lattice for the Confinement of Radioactive Cesium: Quantification of the Amorphous Phase Taking into Account the Incommensurate Modulated Character of the Crystallized Part. *J. Solid State Chem.* 2007, *180* (1), 322−330.

(62) Watson, G. W.; Kelsey, E. T.; de Leeuw, N. H.; Harris, D. J.; Parker, S. C. Atomistic Simulation of Dislocations, Surfaces and Interfaces in MgO. *J. Chem. Soc., Faraday Trans.* 1996, *92* (3), 433−438.

(63) Makov, G.; Payne, M. C. Periodic Boundary Conditions in Ab Initio Calculations. *Phys. Rev. B: Condens. Matter Mater. Phys.* 1995, *51* (7), 4014−4022.

(64) Neugebauer, J.; Scheffler, M. Adsorbate-Substrate and Adsorbate-Adsorbate Interactions of Na and K Adlayers on Al(111). *Phys. Rev. B: Condens. Matter Mater. Phys.* 1992, *46* (24), 16067−16080.

(65) Zakaria, S. N. A.; Hollingsworth, N.; Islam, H.; Roffey, A.; Santos-Carballal, D.; Roldan, A.; Bras, W.; Sankar, G.; Hogarth, G.; Holt, K. B.; de Leeuw, N. H. Insight into the Nature of Iron Sulfide Surfaces during the Electrochemical Hydrogen Evolution and CO_2 Reduction Reactions. *ACS Appl. Mater. Interfaces* 2018, *10* (38), 32078−32085.

(66) Santos-Carballal, D.; Roldan, A.; Grau-Crespo, R.; de Leeuw, N. H. A DFT Study of the Structures, Stabilities and Redox Behaviour of the Major Surfaces of Magnetite Fe_3O_4. *Phys. Chem. Chem. Phys.* 2014, *16* (39), 21082−21097.

(67) Santos-Carballal, D.; Roldan, A.; de Leeuw, N. H. Early Oxidation Processes on the Greigite Fe_3S_4(001) Surface by Water: A Density Functional Theory Study. *J. Phys. Chem. C* 2016, *120* (16), 8616−8629.

(68) Santos-Carballal, D.; Roldan, A.; Dzade, N. Y.; de Leeuw, N. H. Reactivity of CO_2 on the Surfaces of Magnetite (Fe_3O_4), Greigite (Fe_3S_4) and Mackinawite (FeS). *Philos. Trans. R. Soc., A* 2018, *376* (2110), 20170065.

(69) Santos-Carballal, D.; Roldan, A.; De Leeuw, N. H. CO_2 Reduction to Acetic Acid on the Greigite Fe_3S_4 {111} Surface. *Faraday Discuss.* 2021, *229*, 35−49.

(70) Tasker, P. W. The Stability of Ionic Crystal Surfaces. *J. Phys. C: Solid State Phys.* 1979, *12* (22), 4977−4984.

(71) Tersoff, J.; Hamann, D. R. Theory of the Scanning Tunneling Microscope. *Phys. Rev. B: Condens. Matter Mater. Phys.* 1985, *31* (2), 805−813.

(72) Vanpoucke, D. E. P.; Brocks, G. Formation of Pt-Induced Ge Atomic Nanowires on Pt/Ge(001): A Density Functional Theory Study. *Phys. Rev. B: Condens. Matter Mater. Phys.* 2008, *77* (24), 241308.

(73) Shields, A. E.; Santos-Carballal, D.; de Leeuw, N. H. A Density Functional Theory Study of Uranium-Doped Thoria and Uranium Adatoms on the Major Surfaces of Thorium Dioxide. *J. Nucl. Mater.* 2016, *473*, 99−111.

(74) Ungerer, M. J.; Santos-Carballal, D.; Cadi-Essadek, A.; van Sittert, C. G. C. E.; de Leeuw, N. H. Interaction of H_2O with the Platinum Pt (001), (011), and (111) Surfaces: A Density Functional Theory Study with Long-Range Dispersion Corrections. *J. Phys. Chem. C* 2019, *123* (45), 27465−27476.

(75) Christensen, A.; Carter, E. A. First-Principles Characterization of a Heteroceramic Interface: ZrO_2(001) Deposited on an α-Al_2O_3($1\bar{1}02$) Substrate. *Phys. Rev. B: Condens. Matter Mater. Phys.* 2000, *62* (24), 16968−16983.

(76) Arya, A.; Carter, E. A. Structure, Bonding, and Adhesion at the TiC(100)/Fe(110) Interface from First Principles. *J. Chem. Phys.* 2003, *118* (19), 8982−8996.

(77) Chen, Y.; Hong, S.; Ko, H.; Kirshner, V.; Wenisch, H.; Yao, T.; Inaba, K.; Segawa, Y. Effects of an Extremely Thin Buffer on Heteroepitaxy with Large Lattice Mismatch. *Appl. Phys. Lett.* 2001, *78* (21), 3352−3354.

(78) Postica, V.; Vahl, A.; Strobel, J.; Santos-Carballal, D.; Lupan, O.; Cadi-Essadek, A.; De Leeuw, N. H.; Schütt, F.; Polonskyi, O.; Strunskus, T.; Baum, M.; Kienle, L.; Adelung, R.; Faupel, F. Tuning Doping and Surface Functionalization of Columnar Oxide Films for Volatile Organic Compounds Sensing: Experiments and Theory. *J. Mater. Chem. A* 2018, *6* (46), 23669−23682.

(79) Postica, V.; Vahl, A.; Santos-Carballal, D.; Dankwort, T.; Kienle, L.; Hoppe, M.; Cadi-Essadek, A.; de Leeuw, N. H.; Terasa, M.-I.; Adelung, R.; Faupel, F.; Lupan, O. Tuning ZnO Sensors Reactivity toward Volatile Organic Compounds via Ag Doping and Nanoparticle Functionalization. *ACS Appl. Mater. Interfaces* 2019, *11* (34), 31452−31466.

(80) Allred, A. L. Electronegativity Values from Thermochemical Data. *J. Inorg. Nucl. Chem.* 1961, *17* (3−4), 215−221.